Optical field instrumentation for characterizing particle sampling sensors

Nicholas Russell Rentsch

Thesis submitted to the Faculty of the
Virginia Polytechnic Institute and State University
in partial fulfillment of the requirements for the degree of

Master of Science
in
Mechanical Engineering

Kevin Lowe, Chair
Wing Ng, Co-chair
Changmin Son

May 7th, 2024
Blacksburg, Virginia

Keywords: Particle ingestion, particle laden flow, particle sampling, X-Ray Fluorescence

Optical field instrumentation for characterizing particle sampling sensors

Nicholas Russell Rentsch

(ABSTRACT)

Particle ingestion in gas turbine applications can be detrimental to performance and pose significant safety concerns. Areas of high sand concentration are hazardous to aircraft, requiring precautions like routine inspections and maintenance. The engine failure modes are dependent on particle composition, concentration, and size. Particles containing certain minerals tend to melt and stick to turbine blades, which is known as glazing. Alternatively, particles may erode blades from repeated collisions, or they may fill cooling passage holes. Therefore, it is necessary to develop systems that identify these parameters as particles are ingested. This thesis introduces three separate systems responsible for collecting sand concentration, size distribution, and material composition of sand. A particle visualization technique (ParVis), developed at Virginia Tech, was used to validate two sensors developed by commercial partners. One sensor measures particle size and velocity with a method similar to Laser Doppler Velocimetry (LDV). The second sensor measures particle composition with X-Ray Fluorescence (XRF) by physically sampling particles in a flow. There has been little research on applying XRF to moving particles, so experimental data were collected to demonstrate the effectiveness of the sensor. Detection comparisons between two particle types showed promising outcomes for the XRF. Meanwhile, the ParVis technique was iterated to overcome previous limitations and implemented into the testing process to provide particle concentration measurements. Particularly, improvements led to increased accuracy and reliability of the method such as reducing variance in concentration approximations.

Optical field instrumentation for characterizing particle sampling sensors

Nicholas Russell Rentsch

(GENERAL AUDIENCE ABSTRACT)

Aircraft are constantly ingesting particles into their engines. Those operating in dusty environments are at higher risks of engine failure because more particles are ingested, which cause damage in several ways. As engine manufacturers push the turbine operating temperatures higher for efficiency and emissions, sand particles reach melting temperatures and stick to turbine blades, which results in overheating. Because of the potential risks to life, sand ingestion research continues to provide solutions for improving aircraft safety.

This study explores the capabilities of new sensors to quantify characteristics of ingested particles, including the concentration, size distribution, and material composition of sand. An illumination technique for measuring sand concentration from particle imaging was developed at Virginia Tech. The technique was iterated to overcome previous limitations and improve its reliability during this study. It provides a more accurate depiction of the testing conditions that can be used to diagnose and calibrate sensors. In this case, two sensors issued by Creare were tested, one of which measures size and particle velocity, while the other measures sand composition. The first sensor relies on non-intrusive optical measurements and can be mounted directly to an engine inlet. The second sensor collects particles from the inlet flow and applies X-Ray Fluorescence (XRF) to the moving particles. There has been little research on applying XRF to a flow of particles, so experimental data were critical to demonstrate the effectiveness of the sensor. technique was iterated to overcome previous limitations and implemented into the testing process to provide particle concentration measurements.

Dedications

Although I am forever grateful for the many people have supported me and guided me throughout my life, I wanted to give special recognition and dedication to the following:

To my late grandfather Dr. Samuel Rentsch, who astounded me with his creativity and passion for helping others by developing life saving devices with his degrees in engineering and medicine. Throughout his life, he was devoted to the betterment of society by inventing early CPR machines, life preserver suits, and submersible research vessels. I aspire to use my skills to better the lives of others the way he did.

To my late grandfather Eugene Plishevsky, who dedicated his life to his family, immigrating to the US where he had to learn English, farm, build houses and highways, work in machine shops, and more. He made a commitment to provide his family the best opportunity to prosper through countless sacrifices. His greatest achievement was the success of his children and grandchildren, who attended universities and continue to prosper. He set an example for the family that I hope to live by and pass on.

To my father James "Rusty" Rentsch, who gave me the curiosity of how things work. That simple curiosity is why I have a passion for engineering and am always wanting to learn. He introduced me to this field, but never pushed me to be an engineer. I also want to thank him for not naming me Allen Rentsch, as I would have had a more difficult time in school than I already did. I hope he will recognize the impact he has had on my life, more than just my sense of humor. Without him, I may not have found a career that I enjoy working in and learning about.

To my mother Anya Rentsch, who gave me the drive to be successful and make the best of every opportunity I encounter. I would not have survived the long nights it took to get here if she didn't remind me how many sacrifices were made for me to receive a higher education. She made me grateful for the life I have been given and not take things for granted. It made me resilient and have the work ethic that was required during my time in college.

To my girlfriend Amberly, who makes the long hours seem a little shorter, the stress more tolerable, and the success shareable. I am surprised every day by her kindness, humor, and love. Especially on days when I am a little grumpier than usual, she finds a way to make me smile. Without her, I would not have a purpose so clear, and there would be fewer things to look forward to.

"I shall be telling this with a sigh
Somewhere ages and ages hence:
Two roads diverged in a wood, and I—
I took the one less traveled by,
And that has made all the difference."

-Robert Frost

Acknowledgements

I would like to first thank Dr. Lowe and Dr. Ng for their support and genuine commitment to providing an excellent academic experience. Their generosity does not go unnoticed, from offering an opportunity to conduct research at VT and to the time they dedicate to their students. I would like to thank Dr. Gwibo Byun for an extraordinary amount of time he spent working with me in the lab and reviewing my findings as I would not have half the understanding of the work I was doing without his expertise. I would like to thank Dr. Son for his guidance on my thesis topic and providing perspective on life after academia. I am very grateful for his support. I would like to thank Dr. Adit Acharya, Dr. Kris Olshefski, Jubel Kurian, and Pranay Patel for their contributions to my work, whether providing help in the lab or mentorship during my first semester at VT. I would like to acknowledge the contributions of Randall Monk, Jason Doby, Sherry Gong, and Diana Israel. They are fundamental to the success and operation of research programs within Aerospace and Mechanical engineering departments, as well as the ongoing work at the Advanced Propulsion and Power Lab. Thank you to the team at Measurement Science Enterprise and Creare for their assistance and support of the program.

Table of Contents

List of Figures

List of Tables

Abbreviations

AFRL	Air Force Research Lab
APPL	Advanced Power and Propulsion Lab
ARD	Arizona Road Dust
ATD	Arizona Test Dust
DOE	Diffractive Optical Elements
EDX	Energy Dispersive X-ray fluorescence
HSWT	High Speed Wind Tunnel
IBF	Inlet Barrier Filter
IPS	Inertial Particle Separator
LDV	Laser Doppler Velocimetry
OPS	Optical particle Sizer
ParVis	Particle Visualization
PIXE	Particle-Induced X-ray Emission
PSD	Particle Size Distribution
ROI	Region of Interest
VTS	Vortex Tube Separator
XRF	X-Ray Fluorescence

1 Introduction

Aircraft and gas turbine generators constantly ingest particles suspended in the atmosphere. At low quantities, these particles pose little risk to aircraft compared to those that operate in dusty environments. Areas such as deserts, beaches, volcanoes, and large bodies of saltwater contain particulates in the atmosphere which can lead to several turbine failure modes. These include blade degradation, particularly in the compressor, and turbine blade overheating. The factors that determine which failure mode will occur include turbine inlet temperatures and particle material composition.

Particles containing silica tend to erode blades due to their sharp edges and hardness, whereas other particles with low melting temperatures will clog the cooling holes in turbine blades and glaze over. Once these cooling passages are obstructed, blades can exceed their thermal stress allowance and deform. In compressor stages, particles can accumulate on the blades and reduce their aerodynamic performance (Figure 1.1). Helicopters and power generators can experience extreme conditions of sand ingestion during takeoff or landing and dust storms respectively. Current solutions include installing filters called vortex tube separators and inertial particle separators. It is important to know these systems are not perfect and engine health should still be monitored. There have been occasions where gas turbine generators fitted with vortex tube separators failed due to sand ingestion following intense dust storms in the Middle East [1]. Therefore, alternative methods to preventing engine failure must be explored.

Several techniques have been developed to monitor particles at the engine inlet and take in-situ measurements. Intrusive sampling probes can provide estimates of sand concentration and collect particles for chemical analysis. Laser and imaging techniques can determine sand concentration, shape, and particle size distribution (PSD) without interfering with the inlet flow.

The advantages of installing particle monitoring systems are aircraft safety and reduced operation cost. Gas turbine engine failures can lead to significant expenses including the cost of the engine, maintenance, and loss of potential revenue. Currently, engine maintenance is set to standard intervals set by engine manufacturers for life limited parts instead of on a case-by-case basis [2]. This can lead to unnecessary maintenance or neglect. In addition to financial incentives, sensors provide added safety to aircraft operators. It is important to ensure the accuracy of these sensors through validation.

Validating engine sensors presents several challenges. The first is with recreating realistic testing conditions and the second is developing independent tools to cross examine results. Diagnostic instruments allow users to not only validate sensors, but also provide opportunities to calibrate instruments. This paper presents an experimental evaluation of a field instrument that is used to validate particle ingestion sensors.

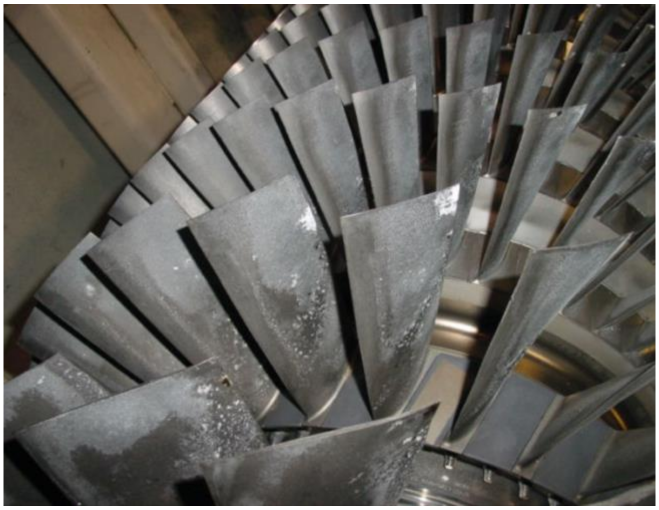

Figure 1.1: Salt deposits on compressor blades [3]

1.1 Outcomes

The objective of this study is to improve the accuracy and reliability of a particle visualization system by capturing data that was unobtainable in previous work. With improvements to the method, it can be incorporated into experimental tests that support validation and calibration of sensors developed by Creare. These sensors can then be fitted to engine inlets for further testing and later onto operational aircraft. Testing the sensors to approximate realistic conditions involved improving the sand delivery platform used at the Virginia Tech Propulsion and Power Lab. In order to determine the success of these objectives, a set of requirements must be met:

1. Develop a testing apparatus to simulate realistic particle ingestion characteristics.
2. Measure local sand concentrations to meet sensor requirements.
3. Advance the current particle visualization processing program.
4. Conduct sand delivery system tests with particle laden flow.
5. Cross examine sand concentrations and particle velocity measurements to validate the sensors.

2 Background

2.1 Atmospheric Conditions and Significant Risk to Aircraft

As the aviation industry continues to grow in technological innovation and aircraft production, so does the emphasis on safety. According to the Bureau of Transportation Statistics, the number of turbine rotorcraft, which are more susceptible to sand ingestion than fixed wing aircraft, has nearly doubled since 2003 [4]. In the middle east alone, the number of commercial aircraft in service is expected to double by 2040 [5]. These aircraft are particularly prone to engine failures as they operate in an area that is the second largest contributor of atmospheric dust in the world [6]. Understanding when aircraft are at the greatest risk of failure is important to identify.

During takeoff and landing, aircraft experience the highest concentration of particulates as they are pulled from the ground. This is known as "brownout" and as the name suggests, a large dust cloud can envelop the aircraft with potential severe consequences. Although fixed wing aircraft can experience brownout, it is often associated with rotorcraft. Similar conditions are experienced by gas turbine generators during dust storms. Therefore, many gas turbine generators and rotorcraft have vortex tube separators installed at the inlet, which filter out particles. Fixed wing aircraft are not fitted with these filters and do not have means of protecting the engine from debris.

The quantity of sand ingested is not the only factor in estimating potential engine damage. Material composition plays a significant role in the severity of damage and the damage mechanism. For example, two squadrons of helicopters operating in Saudi Arabia experienced different levels of degradation due to their geographic location, despite having similar maintenance schedules. The distinction was associated with the chemical mixtures of sand in each region [7]. Even with evidence of engine failures due to high sand concentration and awareness around different failure modes from material composition, there are no certifications for engines that work in dusty conditions.

The push for higher efficiency and higher engine operating temperatures have led to more cases of hot corrosion and glazing damage from molten sand. Molten sand deposits have been found at temperatures as low as 1150ºC depending on their mixtures. For reference, the Rolls Royce Trent 900 has turbine inlet temperatures exceeding 1700ºC [8]. Although not all engines will operate near these high temperatures, they still exceed melting temperatures for common sand mixtures. The other cause of damage is from cooling passage fouling and blade erosion. Ingesting particles at concentrations above 10 mg/m^3 poses an accumulation hazard, and particles can erode compressor blades [9]. Other dusts, such as volcanic ash, have been found at the roots of turbine blades, resulting in overheating and deterioration of thermal coatings.

2.2 Solutions to Reducing Particle Ingestion

Several methods for reducing particle ingestion are currently in practice. Vortex tube separators (VTS), inlet barrier filters, and inertial particle separators aim to filter out particles before they reach the engine inlet. Inlet barrier filters are the simplest designs where a porous material, often a woven mesh, is installed upstream of the inlet. Particles are captured in the mesh, while clean air can pass through. Although they have a high separation efficiency, inlet barriers can create a large pressure drop that hinders engine performance.

Inertial particle separators rely on momentum to separate particles from the core flow. The inlets are curved such that the particles' inertia cannot overcome the sharp redirection of core flow, but instead will follow a separate channel that leads to the atmosphere. Inertial particle separators have much lower separation efficiencies than other methods due to a large dependance on particle size and flow conditions.

Vortex tube separators are similar to inertial particle separators, where the design takes advantage of inertia to separate particles. However, particles enter a helical chamber to induce rotation. Centrifugal forces push particles toward the outer surface where they enter a separate channel that leads to the atmosphere [10]. The inner flow contains clean air and travels to the engine inlet. As with other methods, pressure drop occurs and some particles remain in the core flow.

2.3 Particle Sampling Probes

A method of measuring sand particles at different locations in an engine is with a physical sampling probe. Recent studies on sampling probes have been conducted at Virginia Tech by Collins and Coulon, and by Kristopher Olshefski [11-13]. The purposes of these probes were to collect samples in a Rolls Royce M250 engine and measure particle size distribution (PSD) and particle concentration. However, these measurements were taken separately from the probes by recording the mass of the sample and with a Camsizer X2 device [11].

A challenge for sampling probes is eliminating bias caused by flow imbalance between the probe inlet and the environment. Depending on their size, particles either follow streamlines closely or will maintain their trajectory. Therefore, the probe should not affect incoming streamlines, and is considered isokinetic. In past studies, pressures of the flow and the sampling probe are monitored with pressure taps so that suction can be adjusted. Furthermore, the sampling sensor in this study monitored probe pressures and volumetric flow rates.

Currently, Hal Technologies offers several options for particle sampling probes that are primarily used for monitoring air quality in clean rooms [14]. However, the HPC301 could be adapted to be a laboratory diagnostic tool because of the claimed capabilities. The laser-based sensor provides particle count, size, and concentration measurements. It is limited to particle sizes between 0.3 and 20 microns and has a flow rate of 0.1 cfm so modifications would need to be made prior to its use in engine related tests.

2.4 Optical Particle Sensors

Optical sensors offer nonintrusive methods of measuring flow characteristics in engines. Methods such as laser Doppler Velocimetry (LDV) use two laser beams to produce a fringe pattern from their wave interference. Particles are illuminated as they pass through the fringes, and the signals are collected by a photodetector [15]. The frequency of these signals can be used to calculate particle velocity with

$$f = 2Vsin(b)/\lambda \tag{1.1}$$

where f is the frequency, V is the particle velocity, b is the half angle between the beams, and λ is the wavelength.

Detectors can be positioned either on the side of the laser emitter or on the opposite side. Placing a detector on the same side as the laser source requires stronger lasers but avoids problems due to blockage. Improvements can be made to this technique with diffractive optical elements (DOEs). Similar to LDV, the elements create a structured light pattern from which particle velocity and particle size can be calculated [16]. However, particle velocity is determined from time-of-flight rather than pulse frequency.

A technique using light scattering and extinction is an alternative method that can be combined to measure particle size and concentration. This technique relies on sets of cameras, placed at angles relative to a laser sheet, to capture light reflections off of particles. Images are used to isolate particles and measure the overall intensity. Separately, extinction laser beams measure intensity drops as particles pass through them, which provides a particle count and mass flow [17].

A particle ingestion probe, called the Advanced Monitoring and Measurement of Sand (AMMoS) sensor developed by Innoveering, presents a compact system to measure particle size, concentration, and composition [9]. Its overall size makes it easily deployable at multiple locations within an engine. For particle detection, the sensor applies light scattering by emitting a laser sheet and monitoring pulses of intensity with two detectors. Particle composition is measured from laser induced spectral profiles, which are functions of wavelength and inputs of electron temperature, electron density, and atomic composition. The probe was validated with a process similar to the ParVis method presented in this paper.

2.5 X-Ray Fluorescence

X-ray fluorescence has been used to measure concentrations of elements present in compounds based on their energies. As elements are irradiated by x-rays, they become ionized and release an inner electron. The atom becomes unstable, forcing an outer electron to fill the space. Now the atom's binding energy is lower in the inner orbital than the outer orbital. Fluorescent radiation is emitted and is lower than primary incident X-rays. Because elements have unique energy transitions between electron orbitals, the fluorescent X-rays can identify the concentration of elements in a sample [18].

Currently, XRF is applied to stationary samples, unless measuring homogeneous gas properties that can be collected in a flow [27]. Common practices for analyzing aerosol particles with XRF rely on collecting samples with a filter. X-rays are then fired at the particle laden filter [24, 25]. Recent products on the market, such as the Horiba PX-375, state that they are continuous particle monitoring systems that can be placed in the field and autonomously sample the air for particulates [19]. The system uses non-woven PTFE filter tape that has a one month replacement interval.

XRF is one technique within Ion Beam Analysis (IBA). Alternative methods for identifying elements are Particle-Induced X-ray Emission (PIXE) and Energy Dispersive X-ray fluorescence (EDX). Instead of emitting high energy photons in XRF, PIXE emits protons or other ions. XRF has a higher penetration depth, while the shorter depth of PIXE makes it a preferred method for layer-by-layer analysis [20, 23]. The methods differ in responses to background noise related to atomic number. XRF performs better with lower atomic number elements, such as those found in sand particles. Although PIXE and XRF are similar techniques, PIXE requires more complex equipment which limits its transportability. Therefore, XRF is a preferred method to deploy on an aircraft.

3 Approach

Objective 1: Develop a testing apparatus to simulate realistic particle ingestion characteristics.

It was important to satisfy certain conditions in the lab that exist in realistic environments because a primary objective of this study was to validate sensors designed for operational aircraft. These conditions include recreating brownout conditions and meeting typical idle inlet airspeeds. This required a sand delivery system with varying mass flow and a rig capable of reaching Mach 0.45. The high speed wind tunnel (HSWT) located at the Virginia Tech Advanced Propulsion and Power Lab (APPL) was chosen because it is a suction wind tunnel capable of operating between Mach 0.05 and 0.55.

Some modifications to the HSWT were necessary to reach a sand concentration similar to brownout conditions. This included reducing the diameter of the test section from 6 inches (15.24 cm) to 4 inches (10.16 cm) for a higher overall concentration. Additionally, sand was injected in the upstream direction and angled towards the test section wall with the sensors. This decision driven by a requirement of a more uniform sand distribution and high sand concentration within the sensors' measurement volumes.

Objective 2: Measure local sand concentrations to meet sensor requirements.

To validate the accuracy of the sensors, multiple methods of measuring sand concentration were implemented. The most basic approximation of sand concentration was conducted with mass flow measurements from the scale and the diameter of the test section. This provided an average local sand concentration. However, the sand distribution inside the test section was non-uniform so this value was not relied upon. Therefore, the particle visualization technique (ParVis) was appropriately chosen to measure local concentrations.

In past studies, ParVis primarily relied on images from a single FLIR camera placed upstream of the particle laden flow to measure sand concentration. Some challenges with a single camera setup are the partial view obstruction by the sand nozzle and capturing reflections off the test section walls. Although having one camera was adequate to capture the concentration near the test section wall, which was the region of interest, it would overestimate the local concentration due to particles that were obstructed by the sand nozzle. A second camera was placed at a slight angle to capture the obstructed regions.

Objective 3: Advance the current particle visualization processing program.

In a prior study by Kristopher Olshefski, a particle visualization technique (ParVis) was introduced to sand ingestion engine research. For testing brown out conditions, further work was needed to process high concentrations of sand. As mentioned previously, ParVis used images of sand in a flow to calculate concentration. Because two FLIR cameras were collecting images simultaneously, changes were needed to the post-processing program written in MATLAB.

A checkered calibration plate was placed in the test section at the location of the laser sheet. Both cameras took images of the plate, and these images were used to align both cameras as well as apply image transformations to negate distortion. Also, the process of filling in the sand concentration into the obstructed regions was developed to minimize the effects of camera aperture variations.

Objective 4: Conduct sand delivery tests with particle laden flow.

As this study relied solely on experimental results, the sand delivery system was installed onto the high-speed wind tunnel, where all the sensor validation tests were conducted. However, to ensure the sand delivery system could reach the required sand mass flow and establish test matrices, a benchtop testing campaign was conducted on a small suction wind tunnel. The suction wind tunnel used an inverted WORX 800 leaf blower with a bell mouth capable of Mach 0.17. With this platform, extensive testing was conducted with all sand particle types to evaluate the effects of humidity, particle size, feed rate, and sand nozzle orientation. A FLIR camera and laser were added to this rig to verify that ParVis can measure high sand concentrations.

Objective 5: Cross examine sand concentrations and particle velocity measurements to validate the sensors.

Each measurement technique required ways of verifying the results independently. Sand concentration was measured with the Optical Particle Sizer (OPS) and Parvis. A mass scale provided the actual sand mass flow, which could also be used to calculate concentration. The OPS recorded particle counts, particle velocity and particle size, while ParVis calculated concentration from mass flow and pixel intensity. ParVis has a calibration factor, which allows users to adjust the calculated mass flow to match the experimental mass flow. The concentration results of both sensors were compared. Particle velocity measurements from the OPS were compared to a velocity profile constructed with a pitot static probe. The velocity profile spanned the entire diameter of the test section to record flow disturbances from the sand nozzle and OPS mounts.

4 Methodology

4.1 Sand Particles

This study examined four sets of particles for the purpose of encompassing a variety of particles that an engine may ingest. Three types of sand and two sizes of glass microspheres were used to test the effects of particle size on detection and validate the XRF on analyzing material composition. The sand was supplied by Powder Technology Incorporated and the glass microspheres were provided by Cospheric [21].

4.1.1 CSPEC

The standardized dust MIL E-5007C or otherwise known as CSPEC, has a large particle size distribution that ranges from a single micron to a millimeter in diameter. The batch used in this study had an average size of 200 µm. It is comprised of 99% quartz and less than 1% of microcline. The density of this particle is 2.65 g/cm^3. These characteristics make CSPEC a coarse dust that can be very corrosive to engine blades.

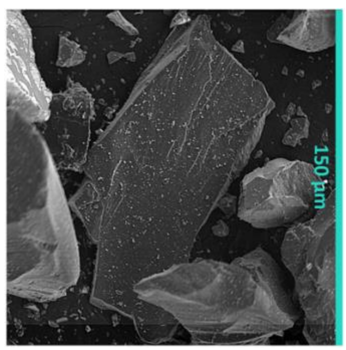

Figure 4.1: Image of CSPEC particles taken by Mark J. Caddick and Alix Ehlers at the Virginia Tech Geosciences Lab.

4.1.2 ATD A4

Arizona Test Dust (ATD) or Arizona Road Dust contains up to 77% silica, 5.5% calcium oxide, 5% potassium oxide, 4% sodium oxide, and 7% iron oxide. This is a common dust used for sand ingestion testing in aerospace and automotive industries. The mean particle size for the batch was 47 µm, and a 90th percentile of 103 µm.

Table 4.1: Chemical Analysis for Arizona Test Dust [21].

Chemical	**% of Weight**	**Chemical**	**% of Weight**
SiO_2	68-76	CaO	2-5
Al_2O_3	10-15	MgO	1-2
Fe_2O_3	2-5	TiO_2	0.5-1
Na_2O	2-4	K_2O	2-5

4.1.3 AFRL-03

Air Force Research Lab test dust is a fine grade powder developed to mimic glazing particles. The dust contains 34% quartz, 30% gypsum, 17% aplite, 14% dolomite, and 5% salt. Its size varies from single micron to over a hundred microns with a mean size of 23 µm. The 90th percentile contained 49 µm particles.

Table 4.2: Chemical Analysis of AFRL03 [21].

Chemical	**% of Weight**	**Chemical**	**% of Weight**
SiO_2	34	$CaMg(CO_3)_2$	14
$CaSO_4 \bullet 2H_2O$	30	NaCl	5
Al, Si, Na, K, Ca	17		

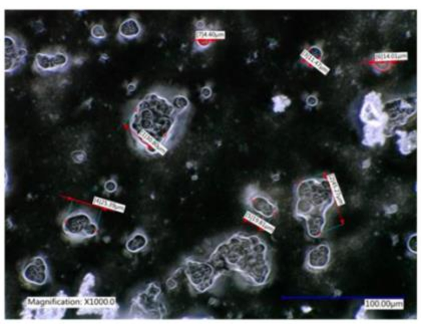

Figure 4.2: Image of AFRL03 [24]

4.1.4 Glass Beads

Two sets of microsphere glass beads were chosen. One set had a mean particle size between 3 to 6 µm while the second set had a mean between 65 and 75 µm. The primary purpose of these beads was to test the OPS sensors accuracy on measuring particle size because the glass microspheres have a tighter size distribution.

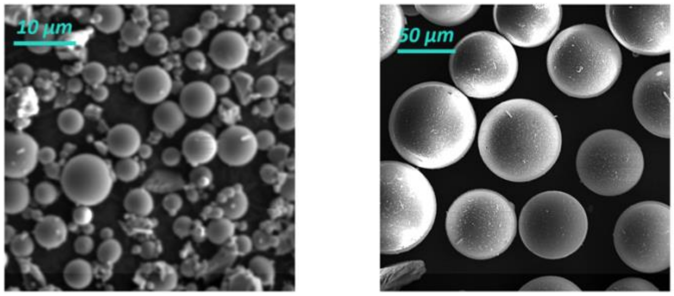

Figure 4.3: Images of glass microspheres, 6 um (left) and 65 um (right), taken by Mark J. Caddick and Alix Ehlers at the Virginia Tech Geosciences Lab.

4.2 Experimental Setup

The experimental setup consisted of the high-speed wind tunnel, sand delivery system, and the sensors themselves.

4.2.1 Sand Feeder

A sand delivery system's purpose was to have controlled transmission of particles into the flow. The system is comprised of an enclosure with the sand feeder, a weight scale, and humidity sensor. All components were placed in an airtight chamber called the purge box. Dry air lines were supplied to the purge box to maintain the humidity below 10%. It was necessary to keep sand particles dry to prevent clumping in the plumbing and in the flow because it could skew the particle sizer sensor. Additionally, particles were baked overnight in an oven to remove moisture they accumulated during storage. These precautions were taken for fine particles like AFRL03 and A4, which had a high tendency to clump. CSPEC did not exhibit clumping. The sand feeder was calibrated for a variety of sands and different feed rates (Appendix A.1).

A sand feeder manufactured by Schenck Process stored particles in a silicone hopper. Particles travel from the sand feeder's hopper to a funnel by a rotating auger and fall into the vacuum conveyor. The mass flow of particles was dependent on the size of the auger and its rotation rate. An external control box allowed the users to set the rotation rate by setting a potentiometer setting, which ranged from 0 to 999. For the purposes of this paper, this value is referred to as the feed rate. The sand feeder sat on top of an Adam Equipment LTB 6002e scale with a resolution of 0.01 grams. Changes to the mass were monitored by a camera.

The ExAir vacuum conveyor relies on a venturi that is controlled by compressed air. According to ExAir, a pressure of 80 psi (552 kPa), the conveyor can produce a vacuum of -4.3 psi (-29.9 kPa). For the tests in this study, the compressed air was set to 30psi. Once particles passed through the venturi, they entered 0.25 in (0.635 cm) flexible tubing until reaching the sand nozzle. The sand nozzle was a 0.25 in (0.635 cm) stainless steel tube that was bent 90 degrees at one end. A 3D printed mount with a rubber seal fixed the sand nozzle to the acrylic test section. The nozzle was pointed upstream at a small angle towards the 3 o'clock position (Figure 4.4).

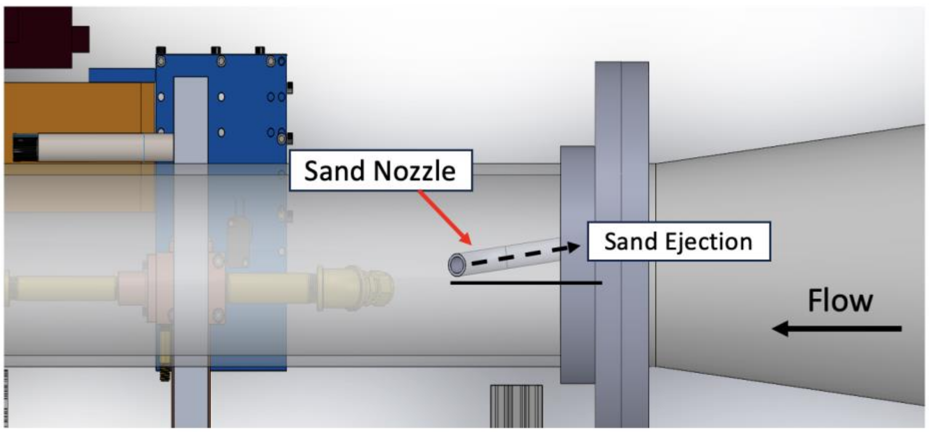

Figure 4.4: Top view of test section showing the angle of the sand nozzle.

4.2.2 High Speed Wind Tunnel

The high-speed wind tunnel is a suction wind tunnel powered by one blower. A flow conditioner is positioned at the inlet of the tunnel, which has a bell mouth secured to it (Figure 4.5). The nominal diameter is reduced from 6 inches (15.24 cm) at the inlet to 4 inches (10.16 cm) at the test section. Two butterfly valves are used to control the flow speed which ranges from Mach 0.05 to 0.55. A pitot static probe measured flow speed in the test section. The test section comprised of a 36 in (91.44 cm) long acrylic tube that was covered by a black film to eliminate ambient light. A slit was cut into the film at the location of the laser plane.

Earlier tests demonstrated the importance of reducing ambient light because it left background image artifacts and increased glare near the test section walls. Other precautions were made to the HSWT, such as shading reflective surfaces and installing laser shields, to prevent secondary light scattering. Vibrations were reduced by adding rubber dampers to the test section mounts and increasing the rigidity of the HSWT frame.

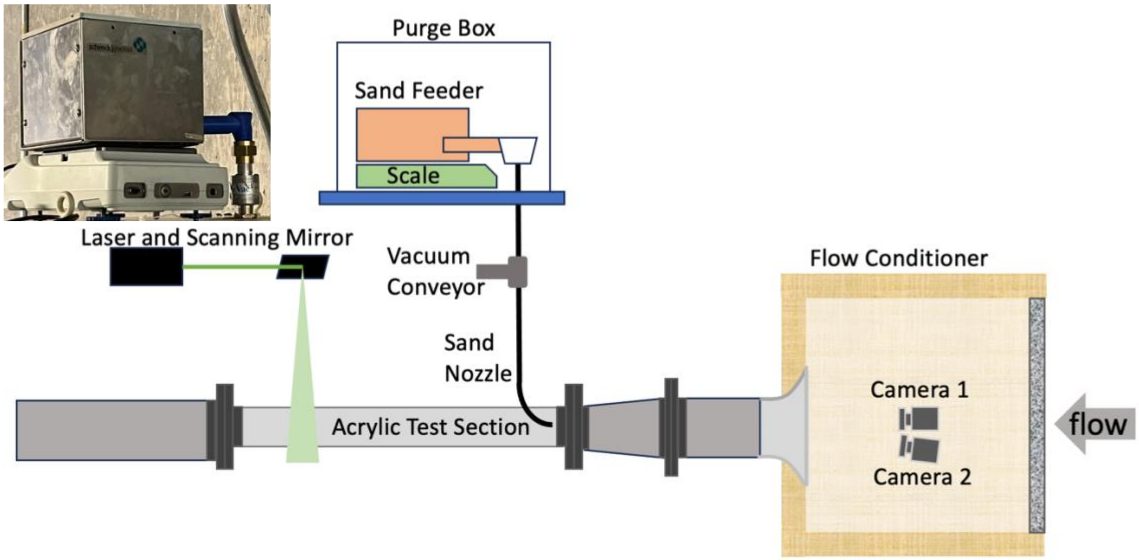

Figure 4.5: Diagram of High-Speed Wind Tunnel.

4.2.3 ParVis

The particle illumination system is comprised of a laser, scanning mirror, and cameras. A 514 nm Coherent Genesis laser was set to 70 mW emitted a beam to a Thor Labs scanning mirror. The scanning mirror oscillated at 100 Hz to create the laser sheet. It was mounted directly above the acrylic test section and the sheet spanned the diameter. Two FLIR Blackfly S-U3-31S4 cameras with 514 nm filters were placed in the flow conditioner.

One camera was positioned along the duct's center axis, and its lens was parallel to the laser sheet. The second camera was placed below the first camera and at a slight angle upwards. This was done to capture areas blocked by the sand nozzle. Both cameras were calibrated with a calibration plate at the laser plane. Both cameras were set to trigger simultaneously to capture identical sand distributions. Images, with a 2048 by 1536 resolution, were captured at 10 frames per second, with an exposure time of 10 milliseconds. This was enough time to develop the full laser sheet.

During each test run, two sets of images were collected by each camera. The first set contained 100 particle free images called background images. It is important to note that the wind tunnel and vacuum lines were turned on while taking these images because the purpose was to minimize the effects of vibrations on the data. Once 100 images were taken, the software averaged the set into one frame. Next, the sand feeder was turned on and another 500 images were taken by each camera referred to as sand images. Both sets were imported into MATLAB where post processing was done. Each sand image underwent background subtraction, where the averaged background image was subtracted from a sand image. These formed a matrix of background subtracted images which isolated the sand particles from artifacts such as glare.

Background subtracted images were analyzed in several ways. The first method involved compiling the 500 subtracted images into a single composite image that would provide the total photon counts in each pixel. With the number of counts, pixel intensity could be calculated and later determine the mass flow of sand; thus, the concentration of particles can be found. These equations will be covered below.

ParVis Calibration

The fundamental model behind ParVis is the relationship between the detected particle count and light intensity of the particles. A detailed discussion and derivation of how the number of scattered photons can be determined from the camera specifications can be found in Olshefski's paper [13]. Based on the experimental setup, he arrives at

$$S_{i,j} = \dot{N}_p \cdot QE \cdot AD \tag{4.1}$$

which equates the intensity count in each pixel to the number of photons per unit time ($\dot{N}_p$), the quantum efficiency of the camera (QE), and the gain sensor conversion (AD). Integrating this value over the region of interest (ROI) would provide the total intensity. Because the total mass flow and intensity are assumed to be directly related, we establish the following equation for a calibration constant:

$$C = \frac{\dot{M}}{\int S_{i,j} dA} \tag{4.2}$$

where $\dot{M}$ is the total mass flow through the ROI. The initial calibration constant is set by measuring the change in mass over time with a precision scale. This can be used with the intensity per pixel to find the mass flow through each pixel with equation (4.3).

$$\dot{m}_{i,j} = CS_{i,j} \tag{4.3}$$

In the previous study, the calibration constant was set with an initial test run and known mass flow. Sequential tests maintained the set calibration constant. However, the tests were at a single Mach number, one type of sand, and a smaller range of sand feed rates. This study explored the performance of ParVis with three sand types, three Mach numbers, and a large variation in feed rates. As a result, the calibration constant was recalculated for each test run using the known change in mass of the sand feeder.

The primary need to reestablish the calibration constant was the relationship between particle velocity and scattering intensity; the faster particles travel through the laser sheet, the lower the scattered intensity. This is due to the exposure time, or shutter speed (t_e), of the camera being longer than the time particles are illuminated by the laser. A particle traveling faster would scatter less light because it is exposed to the laser for a shorter time and therefore would appear less intense. The relationship between the total scattering intensity (I_{Tot}), and particle velocity (V), is described by equations (4.4) and (4.5),

$$I_{Tot} = \int_{t=0}^{t=t_{illum.}} I(\theta)dt \tag{4.4}$$

where $I(\theta)$ is the scattered intensity as a function of the observer angle, and $t_{illum.}$ is the time a particle is illuminated by the laser sheet which is calculated with the width of the laser sheet (L).

$$t_{illum.} = \frac{L}{V} < t_e \tag{4.5}$$

Similarly, larger particles will scatter more light than smaller particles as shown in Figure 4.6. Intensity values were generated with the Fraunhofer Approximation because of the large particle size compared to the laser wavelength [28]. However, the scattering angle was assumed to be small for simplicity of the calculation. As a result, changes to Mach number or particle type will require a recalibration of ParVis. Further analysis and discussion of the calibration factor can be found in Section 5.1.

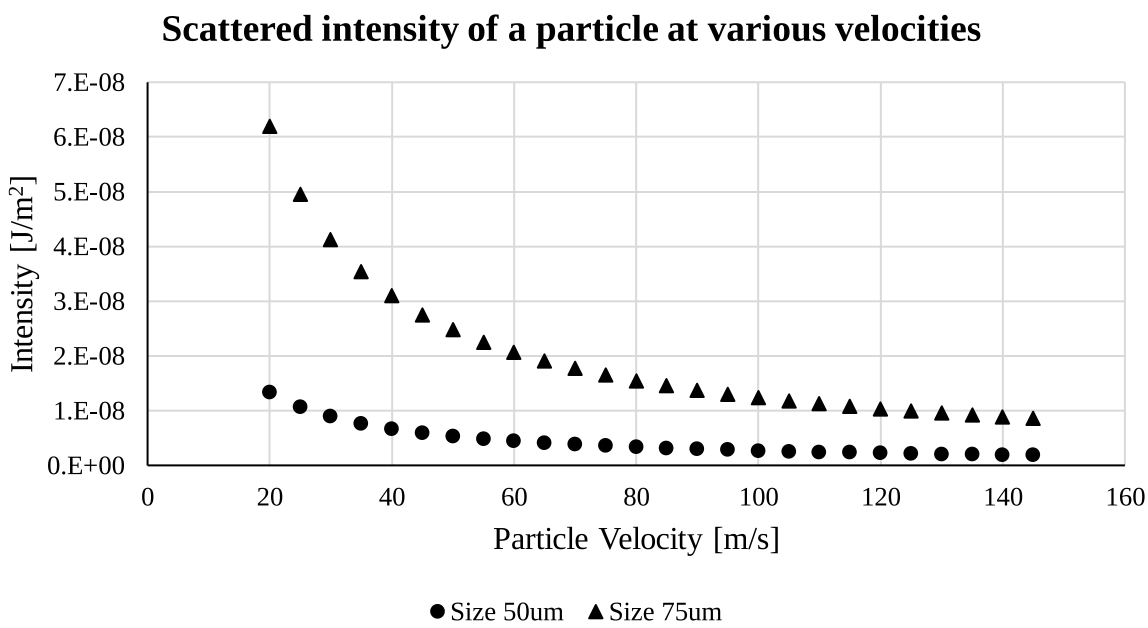

Figure 4.6: Particle scattering intensity as a function of particle velocity for two sizes.

Concentration Calculation

Once the mass flow per pixel is estimated, particle concentration in each pixel can be determined as well as the total concentration. To calculate total particle concentration, the volumetric flow rate of air ($\dot{\forall}_{air}$) was a measured input in

$$\sigma_p = \frac{\dot{M}}{\dot{\forall}_{air}} \tag{4.6}$$

which applied the sand mass flow rate found earlier. The benefit of ParVis is with estimating local concentrations based on local intensity. As a diagnostic instrument for sensor validation, ParVis can select a ROI where point measurements are taken by another instrument and compare local concentrations or mass flows. This is especially beneficial when particles are unevenly distributed in the measurement volume. Therefore, relying solely on equation (4.6) to estimate concentration would yield high uncertainty. Instead, the concentration per pixel was calculated with:

$$\sigma_{p,(\,i,j)} = \frac{\dot{m}_{i,j}}{\dot{\forall}_{air}} \tag{4.7}$$

Image Transformation

Camera calibration is conducted with a calibration plate located at the laser plane. It is comprised of 1 mm^2 black and white squares and completely fills the measurement plane. The plate allows users to focus the cameras and determine the area of a pixel. Furthermore, it is necessary to align sets of images from multiple cameras. Figure 4.7 shows the combined calibration images for two cameras. The bright purple regions show features in only the first camera, while bright green includes features in the second camera. All the areas that are not colored purple or green indicate features present in both cameras such as the squares. Most importantly, the transformation applied to the calibration images was applied to the set of sand images.

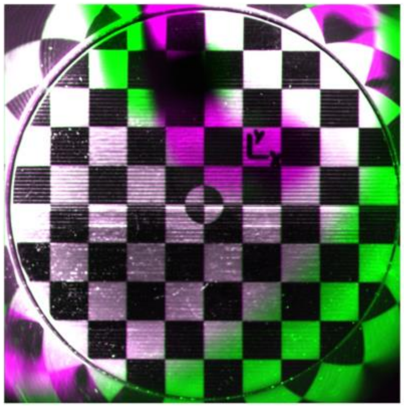

Figure 4.7: Calibration plate alignment for two cameras.

4.2.4 OPS

The Optical Particle Sizer (OPS) was developed by a partnership between Creare and Measurement Science Enterprise Incorporated. Two light sheets are emitted, which are used to measure particle speed and size by time-of-flight. Three lenses are etched into the probe window for the transmitter and receivers (Figure 4.8). Optical fibers carry the signals to a separate processing engine.

Early sensor evaluation was performed to check the optical alignment and test sensor performance. During this stage, a droplet generator was used to test two droplet sizes and velocities. The receiver signals were displayed on an oscilloscope so that hand calculations of particle velocity could be completed. Once benchtop tests were completed, the sensor was shipped to Virginia Tech where it was mounted directly to the acrylic test section.

The OPS was installed with a 0.4 cm step from the duct wall. Its measurement volume of 300um x 250um x 170um was offset by 1.5 cm from the wall. To prevent the OPS window from accumulating particles, a thin air curtain passed over the surface, which was generated from a compressed air supplied.

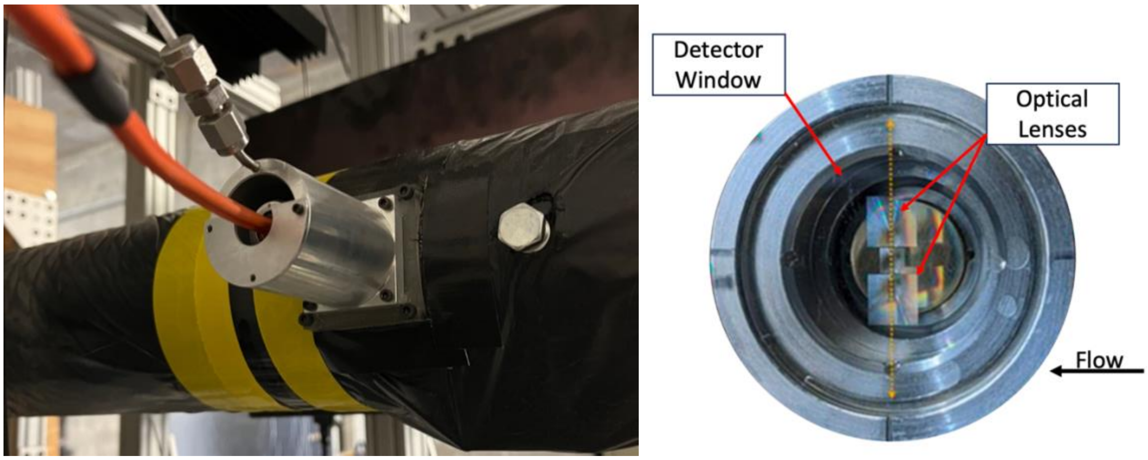

Figure 4.8: OPS sensor mounted to the test section (left) and optical lense locations (right).

Concentration Calculation

The OPS measured particle counts passing through the measurement volume, particle velocity, and particle size. To calculate concentration, the total volume of particles was estimated with,

$$V_{tot.\ particles} = N_{pr} * \frac{4}{3}\pi\left(\frac{d_{particle}}{2}\right)^3 \qquad (4.8)$$

where d_p is the mean particle diameter measured by the OPS and N_{pr} is the total number of particles detected by the OPS. Particle density (ρ_p) was taken from the MSDS provided by PTI. The OPS concentration measurement was approximated with,

$$C_M = \frac{\dot{m}}{Q} = \frac{\rho_{particle} V_{tot.\ particles}}{A_{meas.\ vol} U_{particles} t} \qquad (4.9)$$

taking particle volume from equation (4.8), measured particle velocity (U_p), the time of data collection (t), and the cross-sectional area of the OPS measurement volume (A).

4.2.5 XRF

The X-ray Fluorescence Sensor (XRF) was designed and assembled by Creare. It collects particles in the flow and irradiates the samples with an x-ray tube. Based on the emission of XRF, an x-ray detector generates a spectrum with the number and energy of the x-rays. The spectrum indicates the amounts of elements in the particles. For this paper, the sensor was focused on testing particles with Ca, Si, Cl, and S.

An off the shelf x-ray tube was purchased along with an x-ray detector and power supplies. Particles are collected in the flow by a sampling tube. They travel to a copper measurement chamber and finally into a micron filter (Figure 4.9). The airflow is generated by a venturi vacuum pump and controlled by a series of rotameters. It was important to monitor the flowrate and pressures at different locations to ensure the flow was balanced.

The sensor was calibrated by sampling particle free flows and measuring the energy of argon that was present to set a baseline. If the mean energy of argon did not match the expected value of 2.957 KeV, then the spectrum would be adjusted. Because argon was always detected, its peak would remain consistent when the baseline spectrum was superimposed onto a particle laden spectrum. Any variation to the argon peak, or the presence of other elements, would indicate the sensor required cleaning.

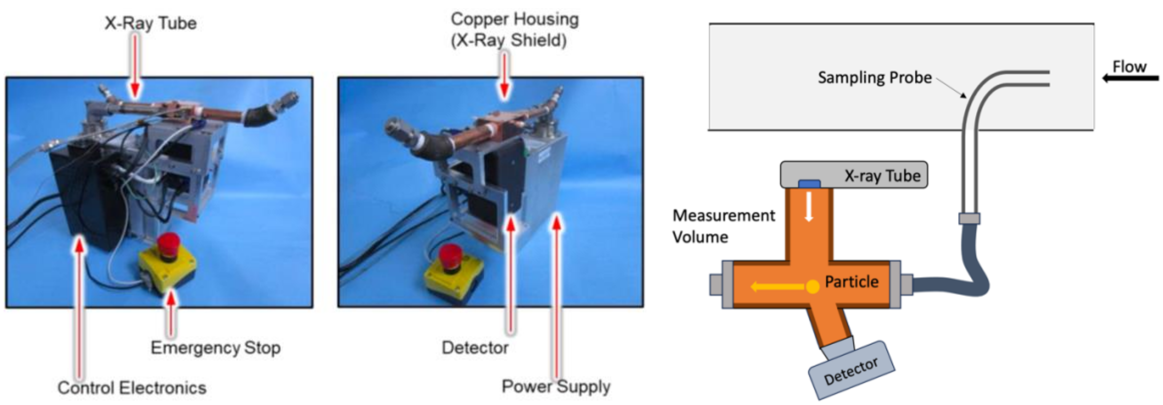

Figure 4.9: Diagrams of XRF sensor.

5 Results and Discussion

The following discussion will cover the results from each of the three sensors. First, results for mass flow and concentration gathered from ParVis will be examined to understand the test conditions for the other two sensors. Next, the section will cover particle size, velocity, and concentration results from the OPS sensor. The last section will report composition results from the XRF sensor.

For each test, five sand feed rates were set at constant intervals. It is important to note that the vacuum conveyor pressure was set to 30 psi (207 kPa) for all Mach numbers, and the decline in sand mass flow with higher Mach numbers is a result of higher stagnation pressures at the sand nozzle.

5.1 ParVis Results

5.1.1 Error and Uncertainty Analysis

An earlier study and development of ParVis by Kristopher Olshefski concluded with a ±6 percent overall uncertainty of the calibration factor [13]. The analysis applied the root-sum-square (RSS) of multiple uncertainty contributions, which considers individual uncertainties and impacts of the contributors rather than an average across all measurements, like in a root mean squared (RMS) analysis. A benefit of RSS is it provides an indication of high sources of error that can then be reduced in future tests with improvements. The RSS analysis was applied to the calibration constant equation by,

$$\delta R = \left\{ \left(\frac{\partial R}{\partial x_1} \delta x_1 \right)^2 + \left(\frac{\partial R}{\partial x_2} \delta x_2 \right)^2 + \left(\frac{\partial R}{\partial x_3} \delta x_3 \right)^2 + \cdots \left(\frac{\partial R}{\partial x_N} \delta x_N \right)^2 \right\}^{1/2} \quad (5.1)$$

where δR is the total uncertainty, $\delta R / \delta x_i$ are the absolute uncertainties, and δx_i are individual uncertainty contributions.

The calibration factor is a function of three parameters: sand mass flow rate, total image intensity, and area of a pixel. Although the same sand feeder and cameras were used in Olshefski's experiments and this study, there were differences to the uncertainties because of the test rig; the distance from the camera and laser sheet, and the vibration level of the mass scale had changed. Mass flow uncertainty was estimated to be ±0.9 g min^{-1} after repeatability tests at different feed rate settings. Camera intensity uncertainty was ±2 percent based on camera specifications [22]. Pixel count was estimated to vary by ±2 pixels after comparing the widths of squares on the calibration plate. With equation 5.1, the total uncertainty of the calibration factor was ±8% at the 95% confidence interval. In the previous study, the uncertainty was found to be ±6% because the mass delivery uncertainty was lower; mass flow was the highest source of uncertainty. This was expected because the mass scale fluctuated with vibrations from the test rig.

Lastly, the nature of sand delivery was influenced by the sand feeder helical mechanism. Although a reasonable time averaged mass flow was obtained, the helix that moves particles into the flow created a periodic delivery instead of steady flow of particles. This behavior resulted in instantaneous mass flows that were much higher than average and could bias the calibration factor in future tests with different sand delivery systems. For example, a steady flow of particles would appear to have lower total image intensities than with periodic flow of the same mass flow rate. Therefore, higher sampling rates are necessary with unsteady sand delivery or calibration testing to determine the calibration factor.

5.1.2 Image Capture

As described in Section 4.2.3, cameras collected sets of images with and without particles. The image in Figure 5.1 shows a background image with the region of interest (ROI). Moderate cropping was done to remove as much glare from the acrylic test section while preserving areas with particles. Although a significant area of the ROI is obstructed by the sand nozzle, further cropping was not conducted because a significant portion of particles would be eliminated. A second camera was added to capture the obstructed region. This reduced the obstructed region from 16% to 3%.

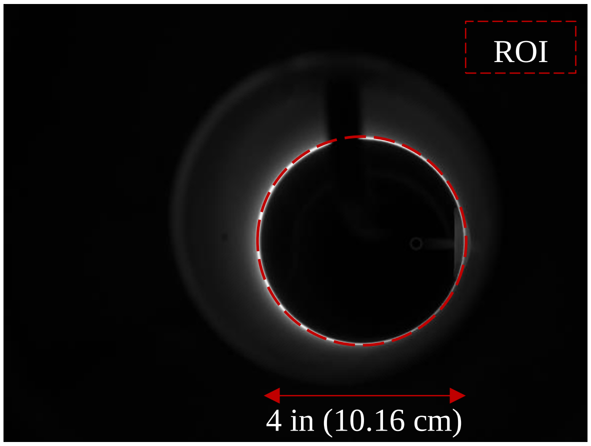

Figure 5.1: Single raw background image with the cropped region of interest shown.

By adding the set of background subtracted images, a composite image was produced that provides the total number of counts and intensity. A threshold was set with Otsu’s method to isolate individual particles from the background. Fully saturated pixels are removed. An intensity contour plot shows regions of high loading at 2 cm to the right of the origin (Figure 5.2).

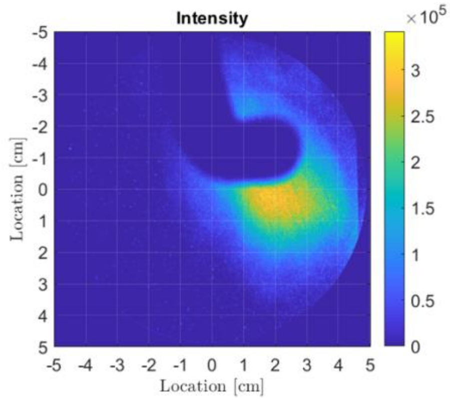

Figure 5.2: Intensity of ARD A4 at Mach 0.25

As mentioned in Section 4.2.3, ParVis was fitted with two cameras to capture the obstructed region. This was particularly important for smaller particles, which remained in the right hemisphere while particles like CSPEC were more evenly distributed across the entire test section. Figure 5.3 shows the comparison of A4 and CSPEC, where A4 remains concentrated near the sand nozzle and CSPEC has an even concentration across the duct. The mean percent difference between the average concentration of the test section and local concentration of the XRF probe was 16% for CSPEC and upwards of 800% for A4. Therefore, a single camera setup was used for CSPEC, and multiple for the other particles.

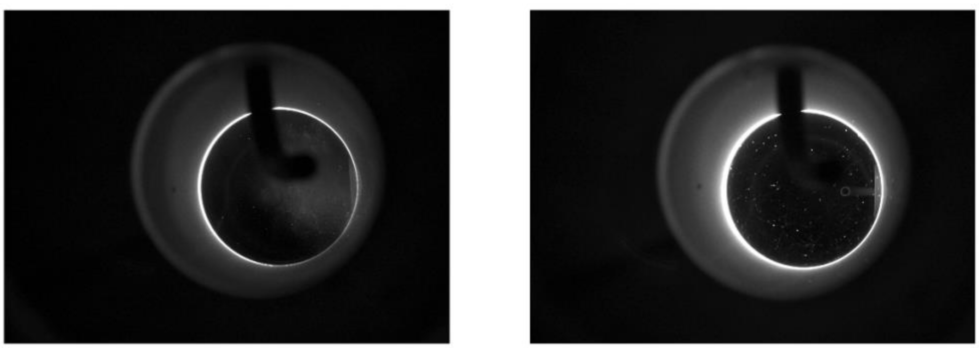

Figure 5.3: Comparisons of sand distribution for ARD A4 (left) and CSPEC (right).

Additional steps were taken to process images from two cameras compared to one camera. Both sets of images were processed independently to develop two composite images containing all sand particles. Next, the obstruction region was isolated in the second camera and spliced into the composite image of the primary camera. Splicing was done by manually finding the corner pixels of the desired cropping boundary. The same pixels were chosen in each camera since the images were aligned. Because there was variation in camera apertures, there would be variation in image intensities. Therefore, a smoothing factor scaled the second camera's intensity in the spliced region.

The smoothing factor was found by calculating the ratio of average intensity between identical regions in the cameras near the spliced area as shown in Figure 5.4. This was verified by plotting concentrations at three heights across the span of the test section (Figure 5.5). The addition of the second camera resulted in improved consistency between intensity and concentration as well as identifying outliers in the single camera data (Figure A.3).

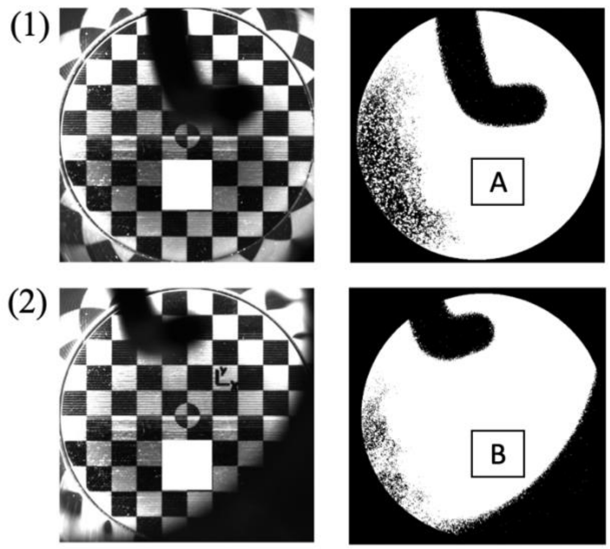

Figure 5.4: Calibration and composite images for camera 1 (top) and camera 2 (bottom).

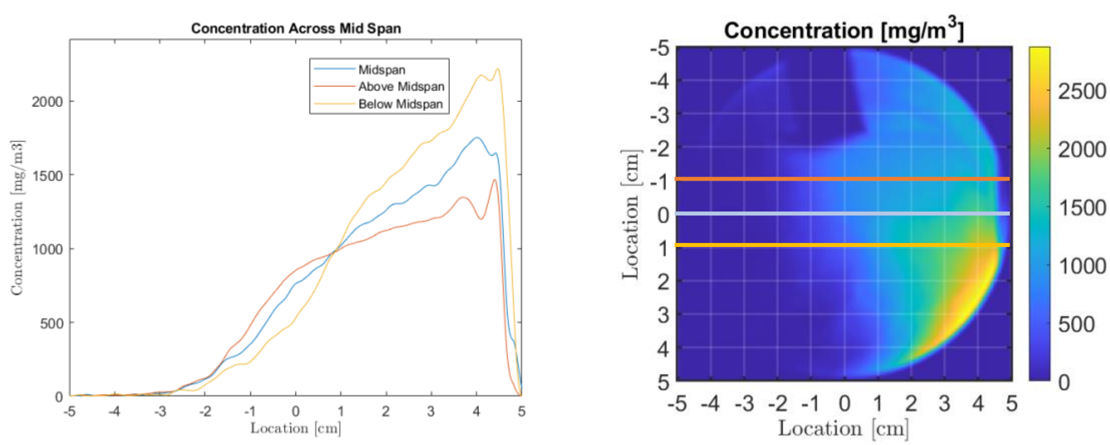

Figure 5.5: Combined camera concentration. Variation of concentration across the span at three heights (left), and contour plot (right).

5.1.3 ARD A4

Arizona road dust A4 was tested at three Mach numbers at five sand feed rates each. As A4 is a finer dust, the sand was more concentrated near the center than near the wall. This can be attributed to the Stokes number which can distinguish particles that will travel with the streamlines or will follow separate paths. Furthermore, Stokes number increases with flow velocity. The contour plots demonstrate this relationship because the region of high particle concentration moves closer to the nozzle exit axis as velocity increases.

The ParVis calibration constant was plotted against the sand feeder mass flow rate in Figure 5.6. As Mach number increases, so does the calibration constant which is expected from equation (4.2) because the intensity will decrease at the same feed rates. However, the increase in mass flow rate should not decrease the calibration constant at the same Mach number.

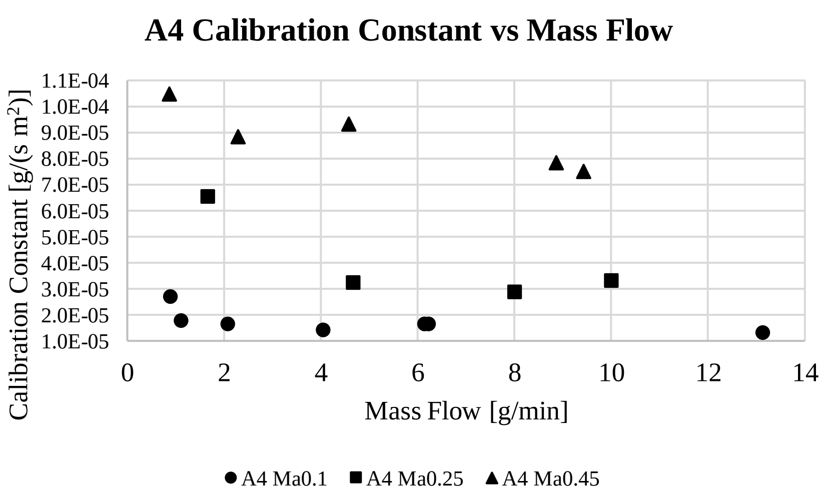

Figure 5.6: ParVis calibration constant relative to Mach number

5.1.4 AFRL03

Testing at three Mach numbers provided interesting behavior with the calibration constant. Similar to ARD A4, the calibration constant increases with Mach number (Figure 5.7). However, the calibration constant does not vary with total intensity at Mach number 0.1 compared to higher Mach numbers. Two sand feeders were used during these set of tests, with the second sand feeder providing more consistent sand delivery and accurate mass flow measurements. The mass flow accuracy of the new sand feeder is the reason for less variation during Mach 0.1 and 0.25 cases.

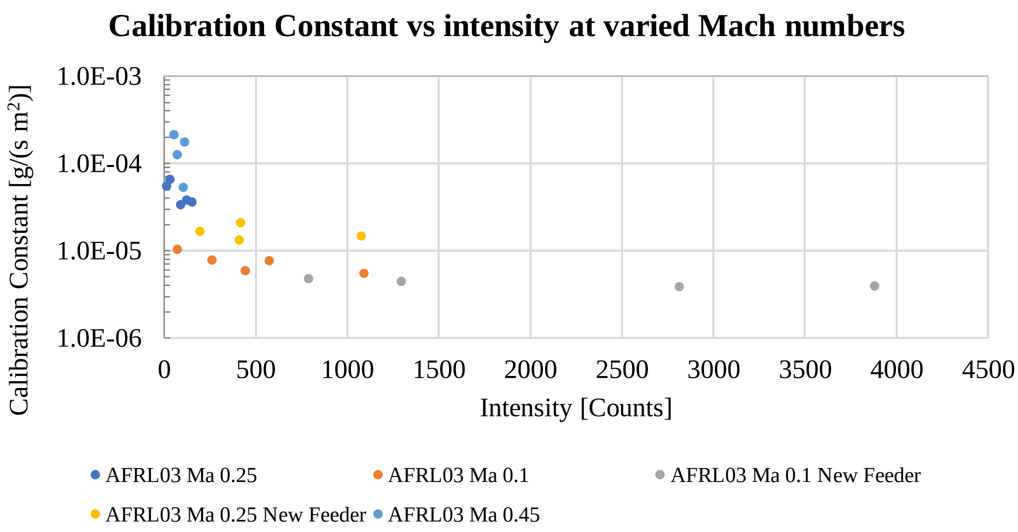

Figure 5.7: Calibration constant relative to the power of the composite image at various Mach numbers.

Figure 5.8 shows the relationship between total intensity of the composite image and the sand mass flow rate is linear as expected from equation (4.3). As Mach number increases, the change in intensity with mass flow decreases until intensity is nearly constant at Mach 0.45. Therefore, the concentration calculation becomes only a function of mass flow rate. This will present challenges if a single calibration constant is set at each Mach number because the calculated mass flow will be constant if the intensity is constant.

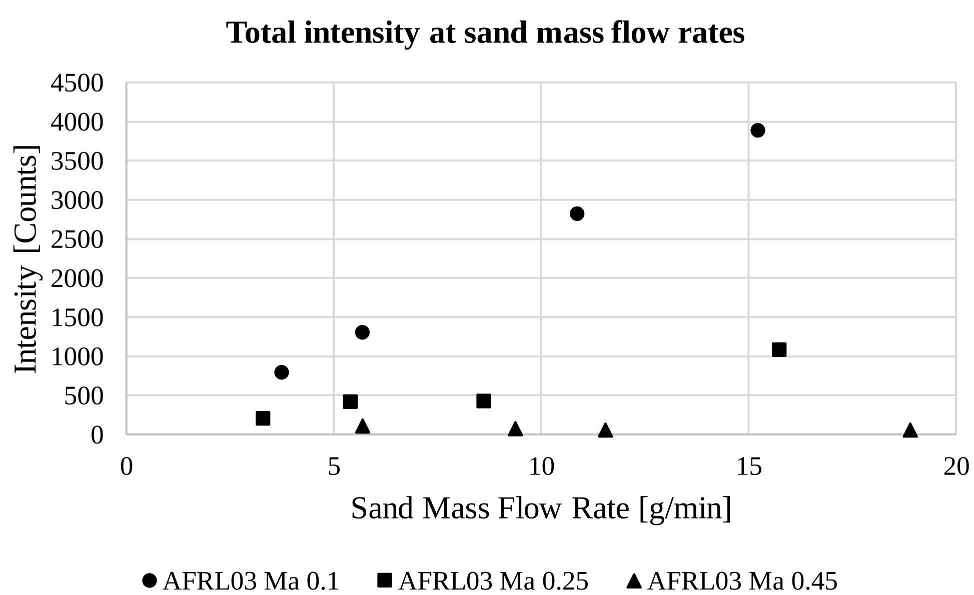

Figure 5.8: Relationship between total intensity and sand mass flow rate at three Mach numbers for AFRL03.

The results in Figure 5.8 suggest that intensity increases linearly with mass flow and at different rates depending on the Mach number. When plotting the calibration constant at Mach 0.1 in Figure 5.9, the curve appears to be exponentially decreasing with mass flow. Similar trends appeared with ARD A4 in Figure 5.6. A repeatability study of ParVis at one Mach number needs to be conducted to see if the trend persists.

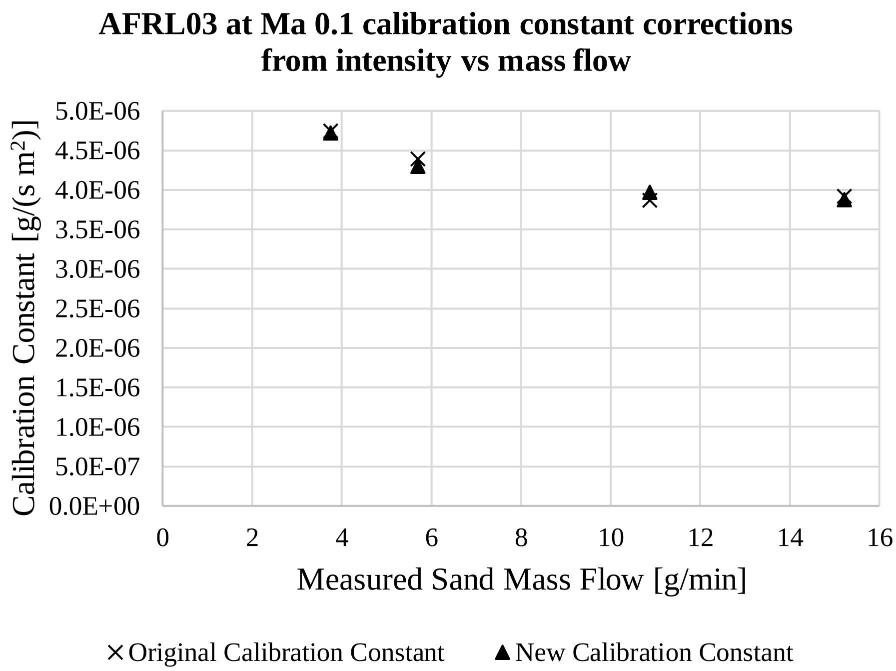

Figure 5.9: A comparison of the original calibration constant for AFRL03 at Ma = 0.1 and the calibration constant generated with the line of best fit from Figure 5.6.

5.1.5 CSPEC

Parvis was initially developed and tested with CSPEC by Olshefski [13]. The large quartz particles are ideal for light scattering techniques. Furthermore, the even distribution of particle across the test section makes it possible to verify ParVis results with simple hand calculations because the average concentration for the duct should be similar to local concentrations in any region within the duct. Figure 5.10 shows a high similarity at Ma = 0.1 and 0.25, while the concentrations differed by 60% at Ma = 0.45. At higher Mach numbers, more particles remained on the side of the sand nozzle.

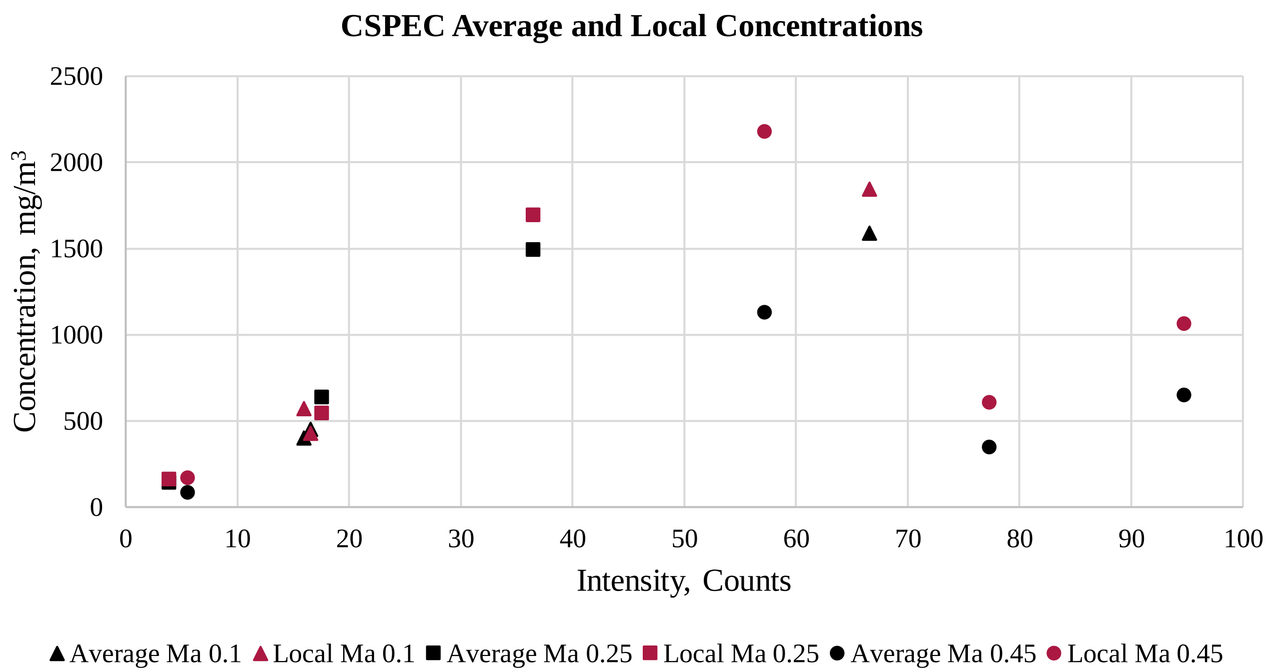

Figure 5.10: Comparing the average concentration of the test section with local concentrations located at the XRF measurement volume.

5.2 OPS Results

The OPS had several constraints which limit the particle size and velocity that could be tested. Particle size was measured between 1 and 100 microns, while particle velocity was measured between 10 and 100 meters per second. Measurements were taken at 50 second intervals.

5.2.1 Velocity and Error Analysis

Velocity measurements of the test section were taken with a Pitot-static probe to plot the velocity profile. Because the OPS sensor has a step near the measurement volume that could affect the flow, measurements were taken with and without the probe installed. Both profiles at Mach 0.1 (Figure 5.11) and Mach 0.25 (Figure 5.12) include the location of the OPS measurement volume.

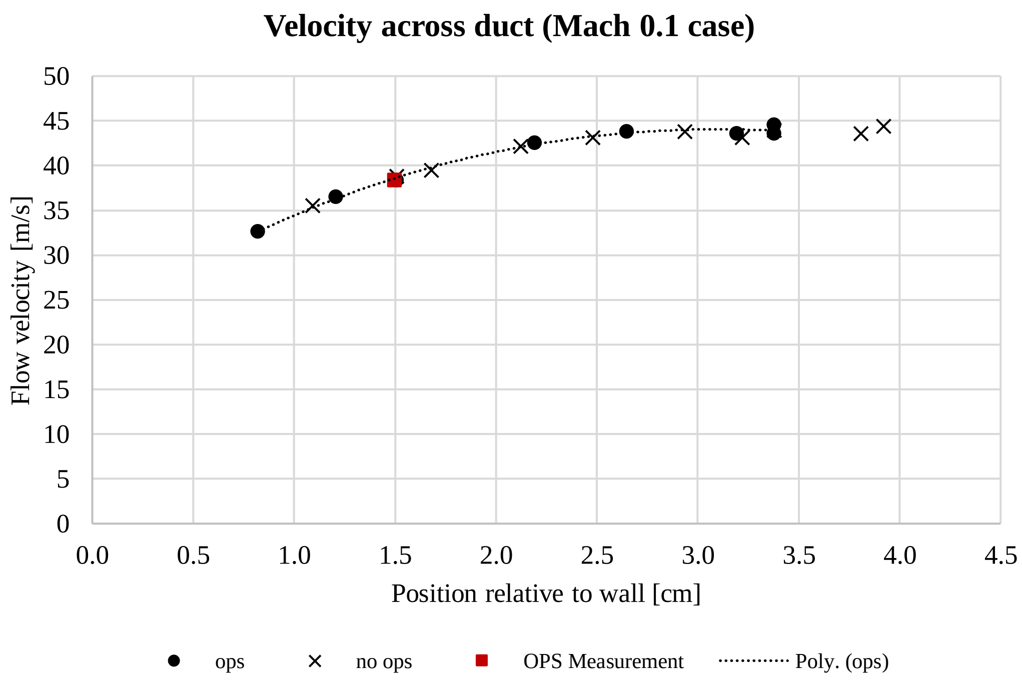

Figure 5.11: Mach 0.1 velocity profiles with and without the OPS sensor installed.

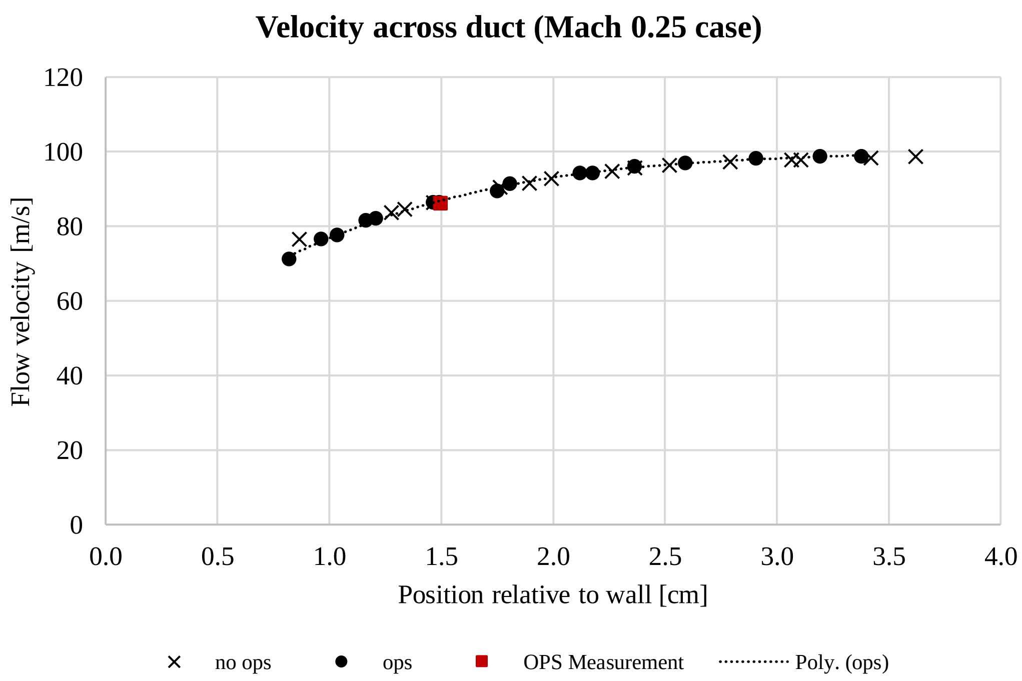

Figure 5.12: Mach 0.25 velocity profiles with and without the OPS sensor installed.

The OPS was tested at five concentrations per each Mach number. Values of mean particle size and velocity were recorded during each run. Table 5.1 shows the averages and standard deviation for each particle and Mach. The OPS velocity measurements show a high degree of consistency across all concentrations and are supported by the pitot probe measurements. Particle size had significant variation with ARD A4, which may be correlated to the wider size distribution compared to AFRL03. The OPS was less accurate in size measurements, although the software has a calibration sizing factor to convert area-based measurements to volume base so that the size distribution meets the sample specifications. Further analysis of each sand batch is needed to confirm the specifications on the MSDS sheets.

Table 5.1: OPS velocity and particle size measurements for ARD A4 and AFRL03 at two Mach numbers.

	A4 Ma 0.1	**A4 Ma 0.25**	**AFRL03 Ma 0.1**	**AFRL03 Ma 0.25**
Average Particle Velocity [m/s]	37.97	86.02	37.72	86.67
Velocity STDev.	0.20	0.23	0.07	0.18
Average Particle Size [um]	45.28	50.27	15.71	18.20
Size STDev.	2.20	1.41	0.14	0.30
Batch Average Particle Size (MV) [um]	47	47	23	23

5.2.2 ARD A4

Local concentrations at the OPS measurement volume were estimated with ParVis and compared to OPS concentrations derived from particle counts. For both Mach numbers, the single camera ParVis setup showed higher concentrations and steeper curves than the OPS (Figure 5.13). However, the ParVis results yielded a closer relationship with both cameras (Figure 5.14). Table 5.2 reports differences between the experimental concentration values to the regression line. At Mach 0.1, the second camera reduced the deviation by 45% and by 79% at Mach 0.25. Some of the outliers present in singe camera data were eliminated by the additional camera.

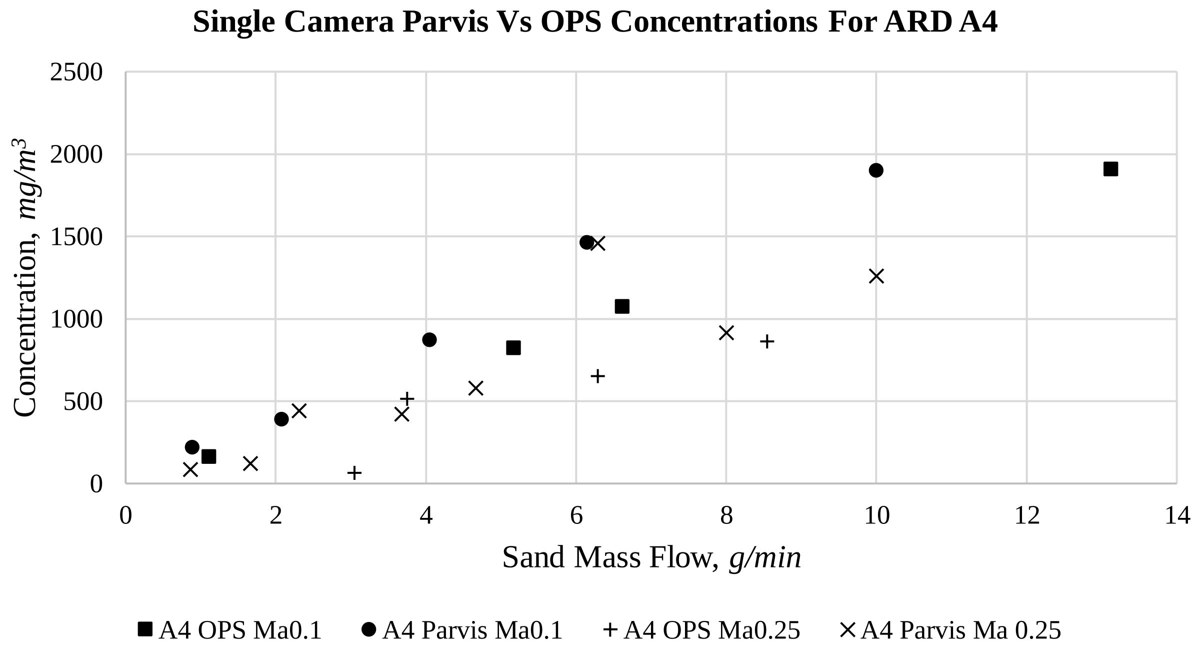

Figure 5.13: Concentration comparison between ParVis and OPS for ARD A4 at two Mach numbers.

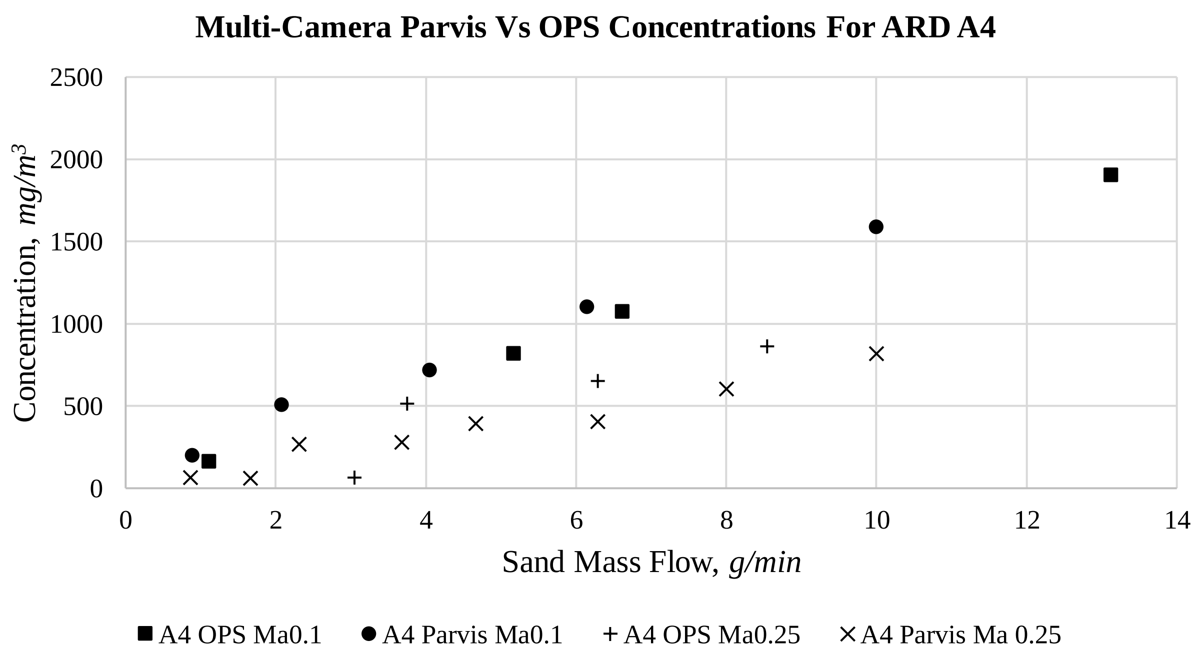

Figure 5.14: Multi-camera ParVis concentrations relative to OPS concentrations at Ma = 0.1 and 0.25.

Table 5.2: Root-Mean-Squared-Deviation of ParVis and OPS concentrations to a regression curve based on the number of cameras.

	Ma = 0.1		Ma = 0.25	
Parvis Cameras	*Single*	*Multi*	*Single*	*Multi*
RMSD of ParVis Concentration to Trendline [mg m^{-3}]	72	39	255	52
RMSD of OPS Concentration to ParVis Trendline [mg m^{-3}]	372	194	323	175

5.2.3 AFRL03

A comparison between ParVis and OPS concentrations shown in Figure 5.15 reports a large difference between both methods for AFRL03. Further investigation is needed to determine the minimum size that can be detected by the OPS, since AFRL03 is a finer sand than ARD. The minimum particle size threshold was set to 1um in the OPS software.

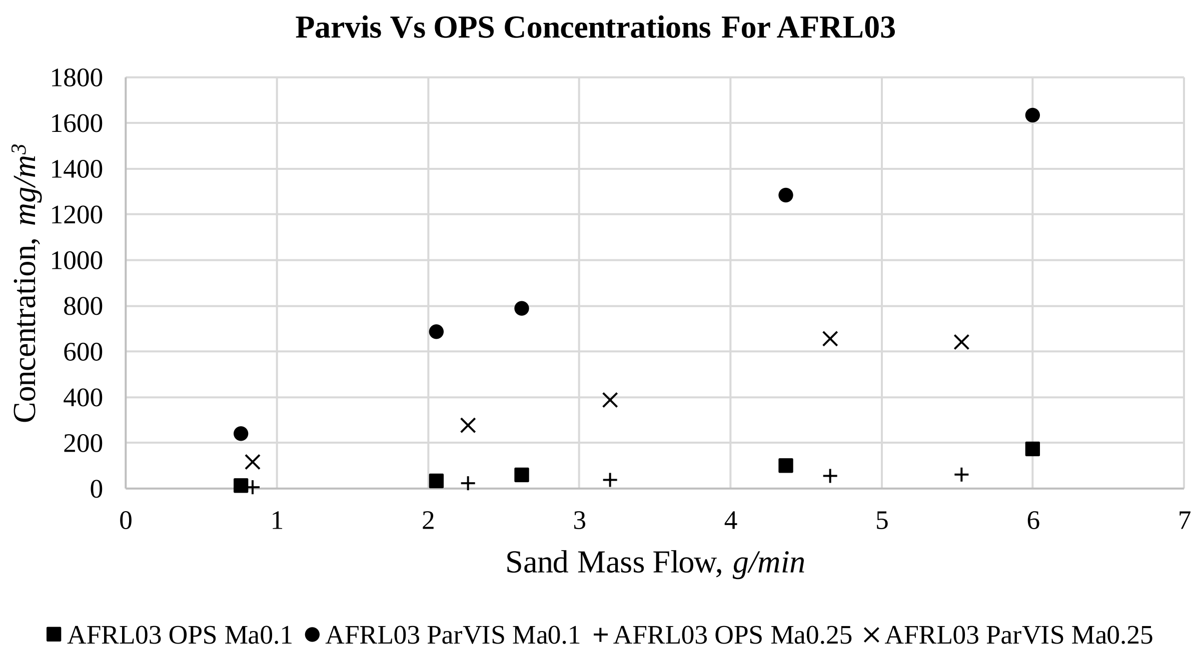

Figure 5.15: Comparison of concentrations between ParVis and OPS at two Mach numbers.

5.2.4 Glass Microspheres

Glass microspheres were tested as a means of calibrating the OPS sensor's size factor. They were preferred for their tight size distribution and uniform spherical shape. Two runs were completed at Ma = 0.25 for each size range and the results are shown in Table 5.3. The smaller size particles had more consistent results for size and velocity than the larger particles. However, the larger particles were tested at two feed rates.

Table 5.3: Velocity and mean size results for two microsphere size distributions at Ma = 0.25.

Manufacturer's Mean Size Range	*3-6 µm*		*65-75 µm*	
Particle Velocity [m/s]	86.78	86.61	85.44	84.53
Mean Size [µm]	14.69	14.91	36.64	40.62
Particle Processed Count	2463	2221	548	67

5.3 XRF Results

The XRF measured counts of trace elements in particles at various energy bands depending on the composition. Each test run was compared to a particle free baseline. All tests and baselines were integrated and normalized by energy bands so that the difference between the integrals would result in the net detection of each element.

5.3.1 AFRL03

The four elements of interest in AFRL03 were sulfur, calcium, silicon, and chlorine. To test the sensor's sensitivity, the sand feed rate was varied to provide a range of concentrations at three Mach numbers. Concentration values were provided with ParVis at the XRF probe location (2.7 cm right of center). At Mach 0.1, the XRF appears to decrease the rate of detection as concentration increases in Figures 5.16 & 5.17, although more testing could reveal outliers in the current data. Another explanation of this trend could be related to Stokes number, where larger particles experience more gravitational force relative to viscous forces of the air at low flow velocities. Remaining particles would be smaller in size and harder to detect by the XRF than large particles. Some literature suggests a strong dependance between XRF signals and particle size for spherical particles [26]. The increase in detection sensitivity as Mach increases suggests a correlation between Stokes number and XRF detection. Two of the four figures can be found in appendix A, although all the figures show similar trends.

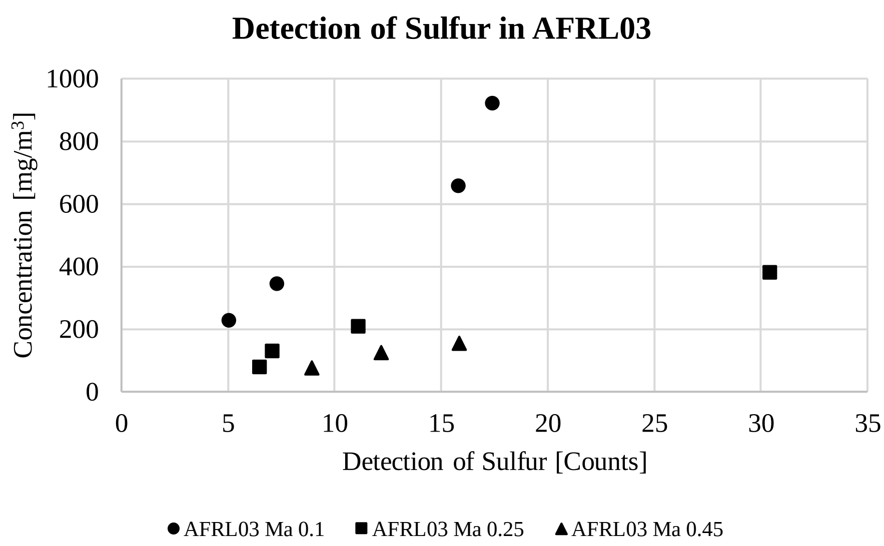

Figure 5.16: Detection of Sulfur in AFRL03 at three Mach numbers.

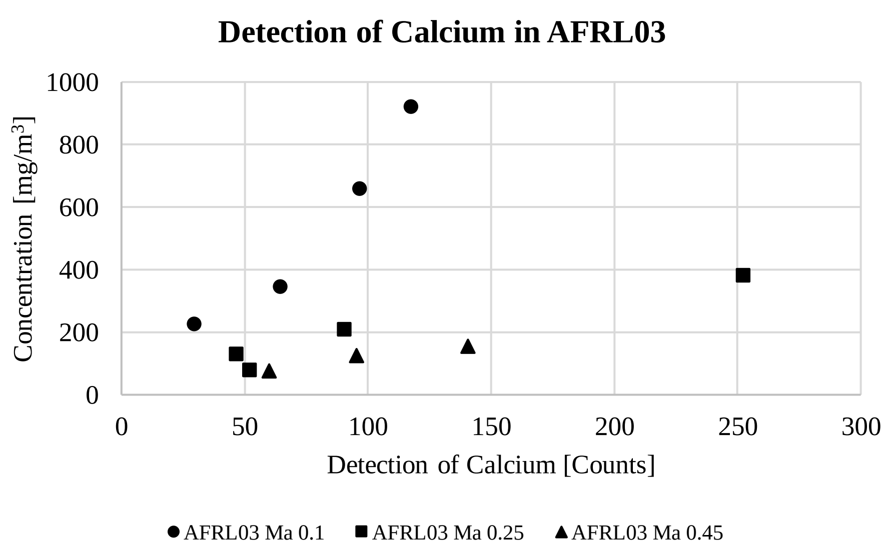

Figure 5.17: Detection of Calcium in AFLR03 at three Mach numbers.

The comparisons to the baseline curve demonstrate that the XRF can successfully identify the four elements of interest in AFRL03. Furthermore, the element detection increases with concentration as expected. Figure 5.18 compares a low and high sand concentration condition at

Ma = 0.1, which shows the increase in detection by the growth of the area under the curves. There were no elements detected that were separate from those on the AFRL03 specification sheet.

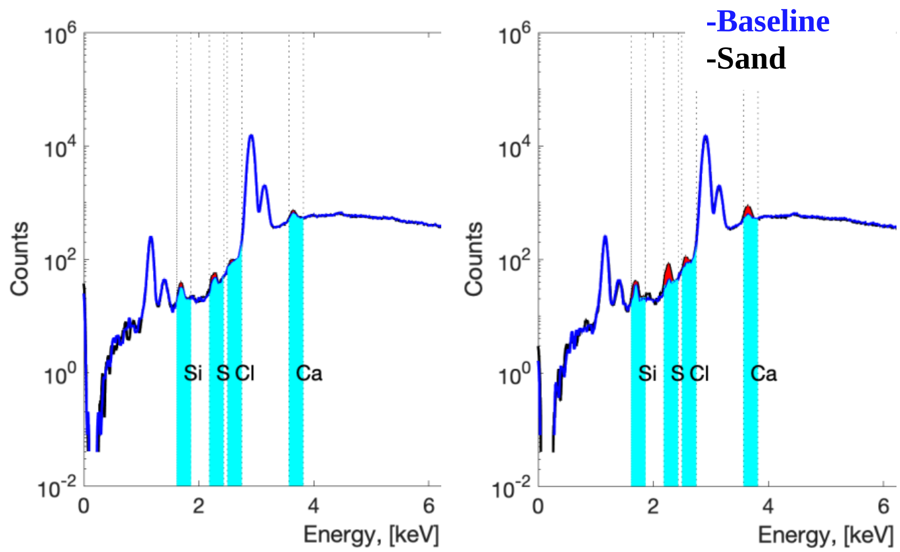

Figure 5.18: XRF sand and baseline comparisons for low concentration (left) and high concentration runs (right).

5.3.2 CSPEC

Compared to AFRL03, the concentration value provided for CSPEC is the total concentration because the particle is more evenly distributed across the entire test section. The detection of silicon in CSPEC was consistent between Mach 0.1 and 0.25 in Figure 5.19, but detection sensitivity increased at Mach 0.45 as with AFRL03. Higher concentrations should be tested to see if or when the XRF has a load limit with CSPEC.

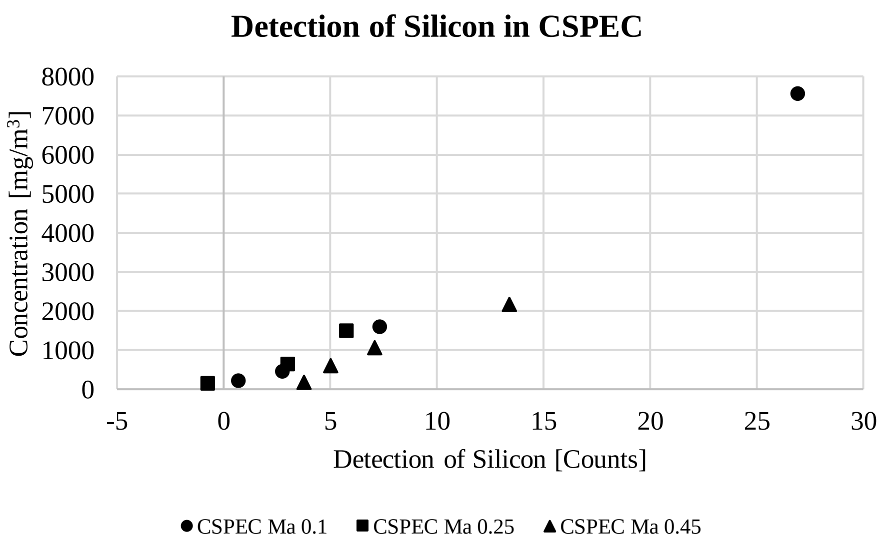

Figure 5.19: Detection of Silicon in CSPEC at three Mach numbers.

As with AFRL03, the sand and baseline curves were compared as seen in Figure 5.20. Since CSPEC is comprised of 99% silica, silicon was the only detection band to appear on the plot.

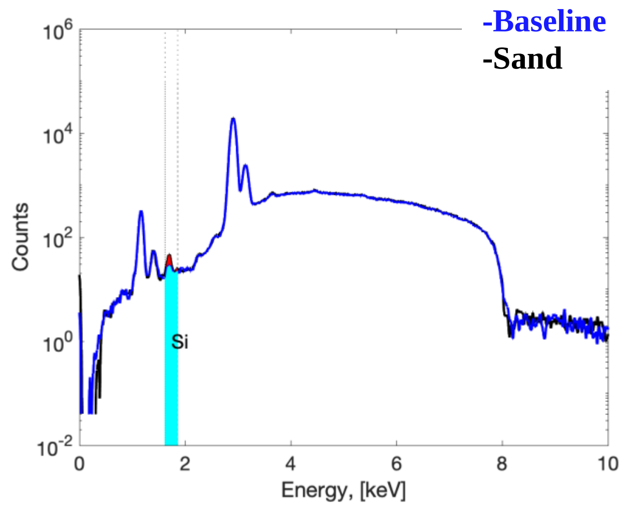

Figure 5.20: CSPEC sand to baseline run comparison for Ma = 0.45.

5.4 Stokes Number and Kinematic Analysis

The behaviors of particles with Mach number in previous sections led to a Stokes number analysis which describes a particles tendency to follow the flow. Specifically, Stokes number is the ratio of a particles characteristic time to the flow characteristic time. A lower Stokes number indicates the particle is more likely to remain airborne in the flow. The Reynolds number for particles was found with,

$$Re_p = \frac{u d_p \rho_f}{\mu_f} \tag{5.2}$$

where d_p is the diameter of a spherical particle, u is the particle velocity, ρ_f is the fluid density, and μ_f is the fluids absolute viscosity. For this study, the Reynolds numbers ranged from 55 to 2185 for the mean particle sizes of AFRL03 and CSPEC. As discussed by Collins [11], the Stokes equation (5.3) is applicable at Reynolds numbers below 1, but a correction factor can be applied at higher Re (equations 5.5 and 5.6). Stokes is determined from characteristic time (t_0), particle velocity (u_0), and characteristic length (l_0).

$$Stk = \frac{t_0 u_0}{l_0} \tag{5.3}$$

$$t_0 = \frac{\rho_0 d_p^2}{18\mu_f} \tag{5.4}$$

$$\psi(Re_p) = \frac{3\left(\sqrt{c}Re_p^{\frac{1}{3}} - \arctan\left(\sqrt{c}Re_p^{\frac{1}{3}}\right)\right)}{c^{3/2}Re_p}; \qquad c = 0.158 \tag{5.5}$$

$$Stk_e = Stk \cdot \psi(Re_p) \tag{5.6}$$

The results of this analysis yielded corrected Stokes values in Table 5.4. Smaller particle sizes in AFRL03 had corrected Stokes values below 1 at Ma = 0.1, while the mean size had a Stk_e of 10. As expected, CSPEC particles had Stk_e numbers above 1 meaning most particles will follow their initial trajectories independent of streamlines.

Table 5.4: Stk_e values for AFRL03 and CSPEC at three Mach numbers.

	Stk_e at Ma = 0.1	**Stk_e at Ma = 0.25**	**Stk_e at Ma = 0.45**
AFRL03 (5 µm)	0.73	1.46	2.20
AFRL03 (23 µm)	10.26	18.21	25.46
CSPEC (20 µm)	8.12	14.57	20.49
CSPEC (200 µm)	313.22	487.41	635.21

An alternative explanation to why the OPS and XRF both had higher detection at lower Mach numbers could be that larger particles experienced larger vertical drops due to gravity at lower Mach numbers. A simple kinematic analysis was done to compare the vertical drops of different particle sizes at different Mach numbers. The time for sand to travel from the sand nozzle and the sensor measurement volumes was estimated by equation (5.7). Because the nozzle was pointed upstream, particle velocity was zero near the nozzle exit. Equation 5.8 provides the vertical drop, where g is the gravitational constant. The vertical drops were found to be 0.3 cm, 0.05 cm and 0.01 cm for Mach 0.1, 0.25, and 0.45 respectively.

$$L = \frac{1}{2}(v_i + v_f)t \tag{5.7}$$

$$dy = \frac{1}{2}gt^2 \tag{5.8}$$

6 Summary and Conclusions

6.1 Summary

- A test apparatus was constructed to conduct particle ingestion research at APPL. This included modifications to previous sand delivery systems and the design of an acrylic test section.
- A particle imaging and illumination technique was inherited and evaluated at multiple test conditions. After assessing its capabilities, further developments were made including a calibration image transformation and splicing images from a second camera to fill obstructed regions.
- Calibration constant correction curves were determined as an alternative method for calibrating ParVis. These will be assessed in future work.
- Using ParVis as a diagnostic tool, the OPS and XRF sensors were tested at multiple Mach numbers, concentrations, and sand particle types.

6.2 Conclusions

- ParVis is shown to provide concentration calculations that were supported by hand calculations and approximations from other techniques for a variety of particles of different sizes. However, the calibration constant must be reestablished for changes to particle type or particle velocity.
- Images from multiple camera angles can be combined to improve the accuracy of ParVis to result in a 5 percent difference between experimental concentration and the regression line. The additional camera reduced the obstructed area in the image from 16 percent to 3 percent. This led to a reduction in deviation from the regression line when using two cameras compared to one.
- The OPS detects particle velocity for particles above 1 μm within a 2 percent error. However, particle detection is limited for particle size distributions similar to AFRL03. For this reason, it was most effective for ARD A4.
- The XRF sensor had detected particles at concentrations above 170 mg/m^3 for CSPEC. For AFRL03, the sensitivity of each element varied with Mach number, although detection frequently occurred at concentrations above 130 mg/m^3. Overall, it was successful in

detecting elements present in AFRL03 and CSPEC, with the detection increasing with concentration as predicted.

6.3 Future Work

- A sensitivity analysis of ParVis calibration constant to determine whether exponential trends between sand mass flow and intensity exhibited in this study are results of secondary light scattering or experimental errors. Testing with structured light could determine the impact of light scattering and glare had on the current results. Furthermore, ParVis should be tested to find the upper limits of sand concentration that it can measure.
- A calibration repeatability study should be conducted to determine the uncertainty due to particle velocity, concentration, and size. The study should identify which elements provide the largest contributions of uncertainty to the ParVis calibration constant that were not considered in this study.
- Improvements to the purge air supply on the XRF sensor will reduce the buildup of particles in the measurement volume.
- Development of the OPS sizing algorithm should be completed to improve sizing distribution measurements.
- Uncertainty analysis of OPS and XRF

References

[1] Tayebi, K., Nair, S., Jupudi, M.M., Dawood, A., & Khalidi, A. "*Sand Ingress in Gas Turbines Operating in Desert Environments: Observations and CFD Simulations.*" Proceedings of the ASME Turbo Expo 2023: Turbomachinery Technical Conference and Exposition. Volume 13C: Turbomachinery — Deposition, Erosion, Fouling, and Icing; Design Methods and CFD Modeling for Turbomachinery; Ducts, Noise, and Component Interactions. Boston, Massachusetts, USA. June 26–30, 2023. V13CT31A006. ASME. https://doi.org/10.1115/GT2023-102745

[2] Ackert, S. Aircraft Monitor. *"Engine Maintenance Concepts for Financiers."* 2011.

[3] Meher-Homji, C., Bromley, F. A., Stalder, J.P. (2013)*"Gas Turbine Performance Deterioration and Compressor Washing."* Proceedings of the 2nd Middle East Turbomachinery Symposium. Doha, Qatar. March 17-20, 2013. Copywrite 2013 by Turbomachinery Laboratory, Texas A&M University.

[4] Bureau of Transportation Statistics. (2022). "*Active U.S. Air Carrier and General Aviation Fleet by Type of Aircraft*."

[5] Bojdo, N., Filippone, A., Parkes, B., Clarkson, R. (2020) *"Aircraft engine dust ingestion following sand storms."* Aerospace Science and Technology, Volume 106, 2020, 106072, ISSN 1270-9638, https://doi.org/10.1016/j.ast.2020.106072.

[6] Tanaka, T.Y., Chiba, M. (2006) *"A numerical study of the contributions of dust source regions to the global dust budget."* Global Planet Change 52 (1–4) (Jul 2006). 88–104, https://doi .org /10 .1016 /J .GLOPLACHA.2006 .02 .002.

[7] Krisak, M.B. (2015) *"Environmental Degradation of Nickel-Based Superalloys Due to Gypsiferous Desert Dusts."* PhD thesis, Air Force Institute of Technology WPAFB.

[8] Rao, A. G., Yin, F. (2017). *"Performance analysis of an aero engine with inter-stage turbine burner."* Delft University of Technology.

[9] Papadopoulos, G., Bivolaru, D., & Siu, S. (2023) *"Sensor System Maturation for Gas Turbine Engine Particulate Ingestion Monitoring."* Proceedings of the ASME Turbo Expo 2023: Turbomachinery Technical Conference and Exposition. Volume 4: Controls, Diagnostics, and Instrumentation. Boston, Massachusetts, USA. June 26–30, 2023. V004T05A033. ASME. https://doi.org/10.1115/GT2023-105793

[10] Acharya, A. S. (2023). *"Aerodynamic interactions in vortex tube separator arrays."* (dissertation). Virginia Tech

[11] Collins, A. S. (2021). *"Development of a novel probe for engine ingestion sampling in parallel with initial developments of a high-speed particle-laden jet."* (dissertation). Virginia Tech.

[12] Coulon, T. A. (2022). *"Evaluation of a particle sampling probe to measure mass concentration in particle-laden flows."* (dissertation). Virginia Tech.

[13] Olshefski, K. T. (2023). *"Development of diagnostic tools for use in a gas turbine engine undergoing solid particulate ingestion."* (dissertation). Virginia Tech.

[14] Hal Technology. (2023). *"Air particle counter."*

[15] Hall, N. (2021). *"Laser Doppler Velocimetry."* NASA.

[16] Wilson, W. W., Gogna, P. K., Chacon, R. J., Muller, R. E., Fourguette, D., Modarress, D., Taugwalder, F., Svitek, P., Gharib, M. (2002). *"Diffractive Optics for Particle Velocimetry and Sizing."* Optical Society of America.

[17] Moon, C., et al. (2021). *"Non-intrusive optical measurements of gas turbine engine inlet condensation using machine learning."* Measurement Science and Technology.

[18] Barth, A., Wirth, K. (2024). *"X-Ray Fluorescence. Geochemical Instrumentation and Analysis."* Science Education Resource Center at Carleton College.

[19] Horiba Process and Environmental. (2024). Products.

[20] Boivin, F., Vallières, S., Fourmaux, S., Payeur, S., & Antici, P. (2022). *"Quantitative laser-based x-ray fluorescence and particle-induced x-ray emission."* New Journal of Physics, 24(5). https://doi.org/10.1088/1367-2630/ac6767

[21] Powder Technology Incorporated. (2023). *"Typical Chemical Analysis for Arizona Test Dust Products."*

[22] FLIR Software Services. *"Emva 1288 imaging performance."* http://softwareservices.-flir.com/BFS-U3-31S4-BD2/latest/EMVA/EMVA.html

[23] Jaksic, M., Paszti, F., Kotai, A., Fazinic, S. (2000). *"Instrumentation for PIXE and RBS."* International Atomic Energy Agency-Physics Section December, 2000.

[24] Ciniglia, D., Cirelli, P., Bilo, F., Zanoletti, A., Cornelio, A., De Iuliis, S., Depero, L. E., Bontempi, E., Perrone, M. G., Lopinto, P., Zonca, M., ; Borgese, L. (2023). *"Characterization of nebulization generated aerosol particles dispersion and deposition by total reflection x-ray fluorescence."* Aerosol Science and Technology, 57(2), 165–174.

[25] Crawford, A. M., Kurecka, P., Yim, T. K., Kozemchak, C., Deb, A., Dostál, L., Sun, C.-J., Brewe, D. L., Barrea, R., ; Penner-Hahn, J. E. (2016). *"Development of a single-cell x-ray fluorescence flow cytometer."* Journal of Synchrotron Radiation, 23(4), 901–908. https://doi.org/10.1107/S1600577516008006

[26] Czyzycki, M., Bielewski, M., & Lankosz, M. (2009). *"Quantitative elemental analysis of individual particles with the use of micro-beam x-ray fluorescence method and monte carlo simulation."* X-Ray Spectrometry, 38(6), 487–491. https://doi.org/10.1002/xrs.1203

[27] Tranter, R. S., Kastengren, A. L., Porterfield, J. P., Randazzo, J. B., Lockhart, J. P. A., Baraban, J. H., Ellison, G. B. (2017). *"Measuring flow profiles in heated miniature reactors with x-ray fluorescence spectroscopy."* Proceedings of the Combustion Institute, 36(3), 4603–4610. https://doi.org/10.1016/j.proci.2016.06.104

[28] Cremonesi, L. (2020). *"Light scattering from micrometric mineral dust and aggregate particles : effects of structure and shape applied to paleoclimate studies."* (Ser. Springer theses). Springer.

Appendices

A First Appendix

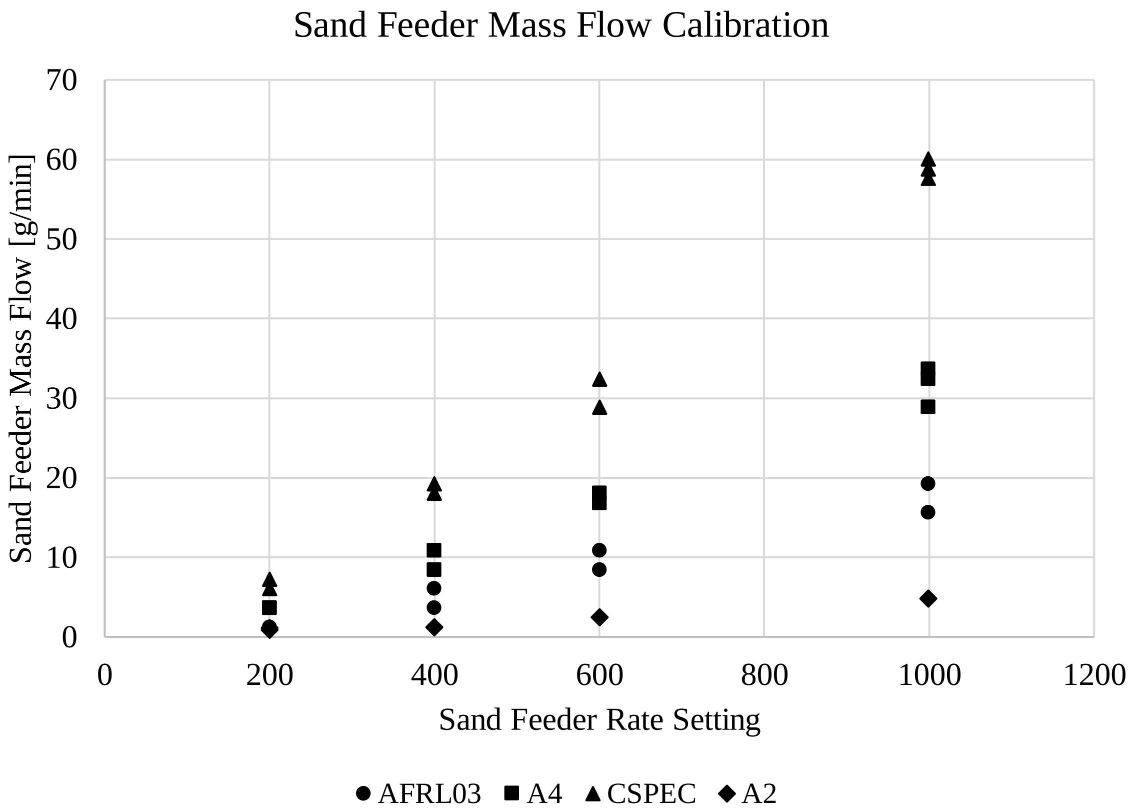

Figure A.1: Sand mass flow rates for each feed rate and particle type.

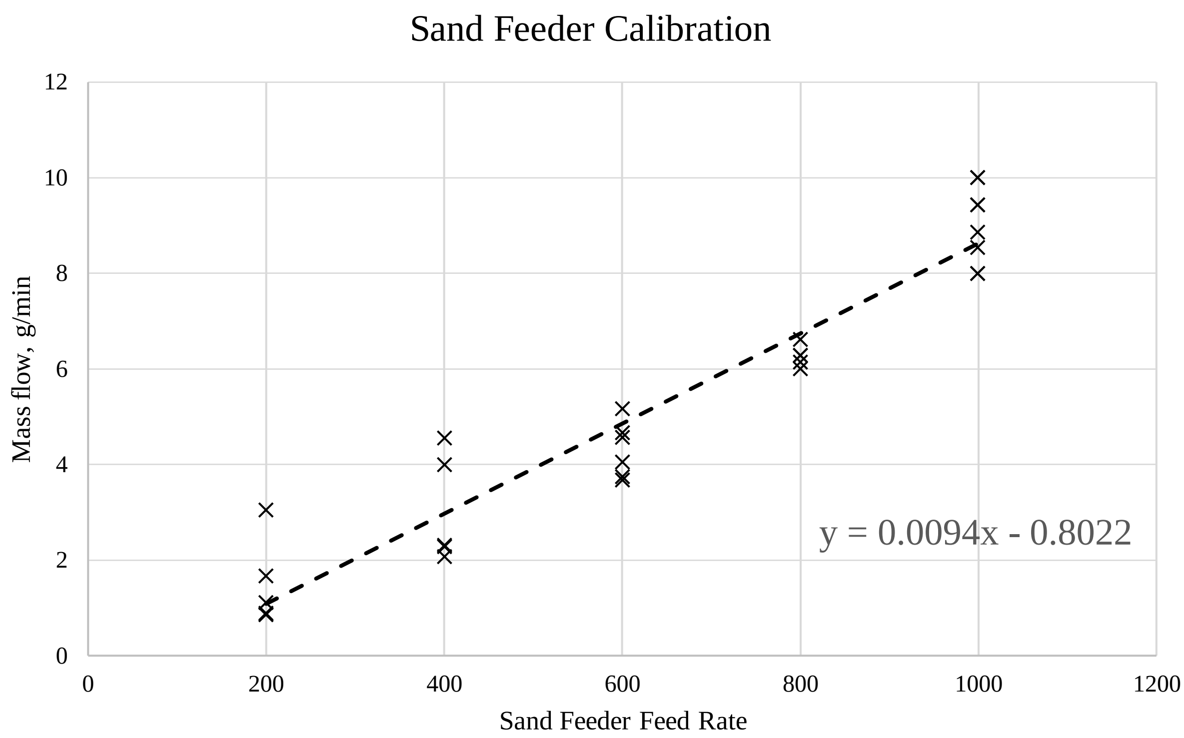

Figure A.2: Sand feeder repeatability study at various feed rates for ARD A4.

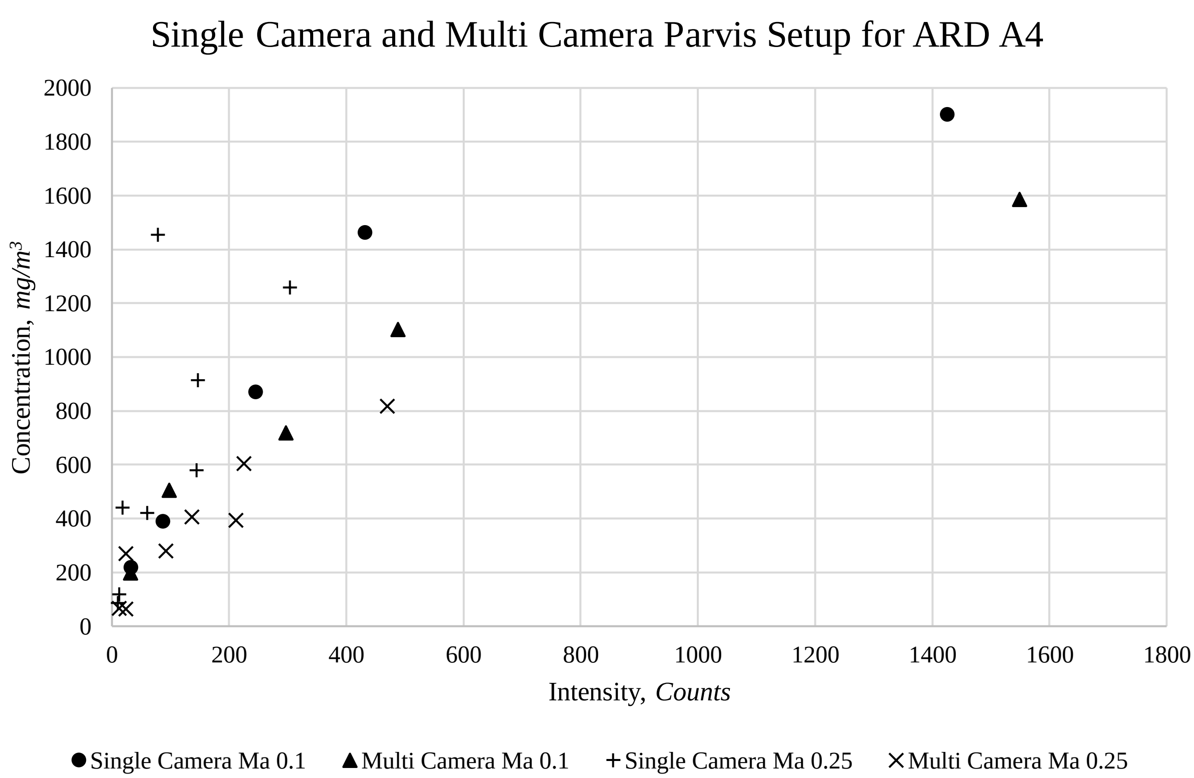

Figure A.3: Comparison of concentrations from single to two camera ParVis.

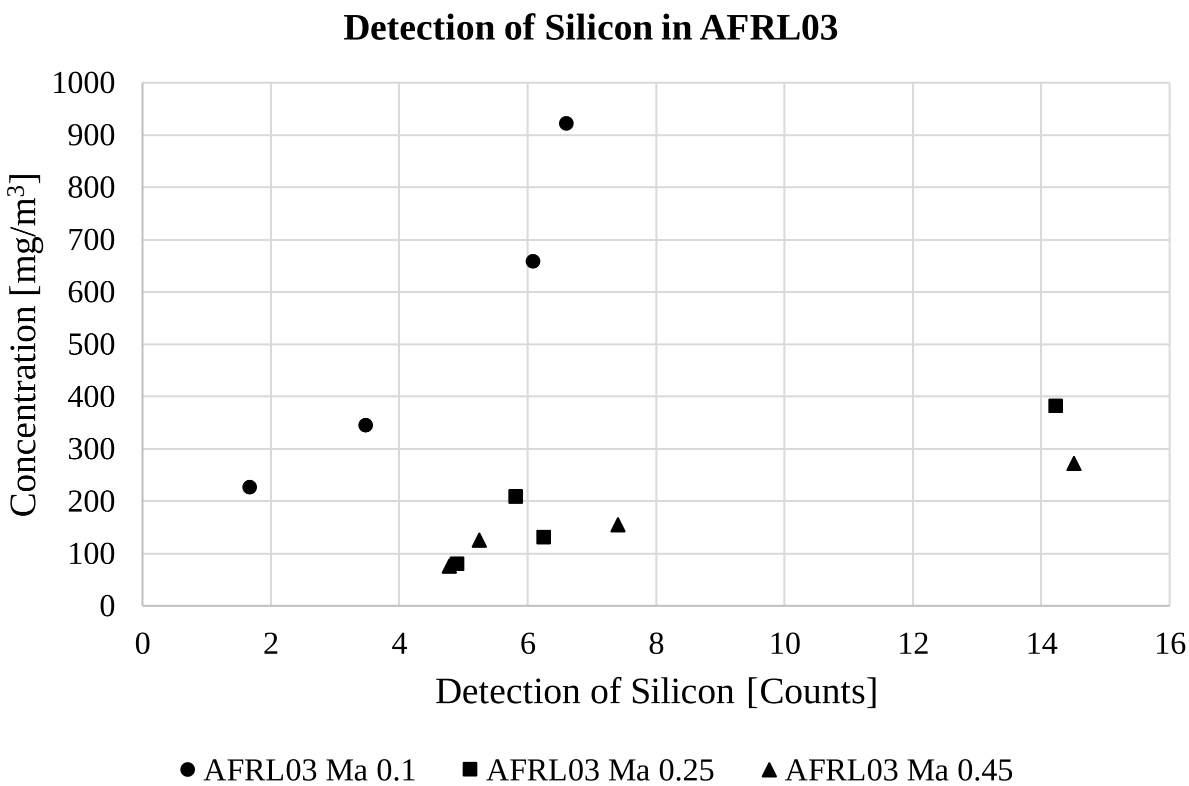

Figure A.4: XRF detection of Silicon for AFRL03.

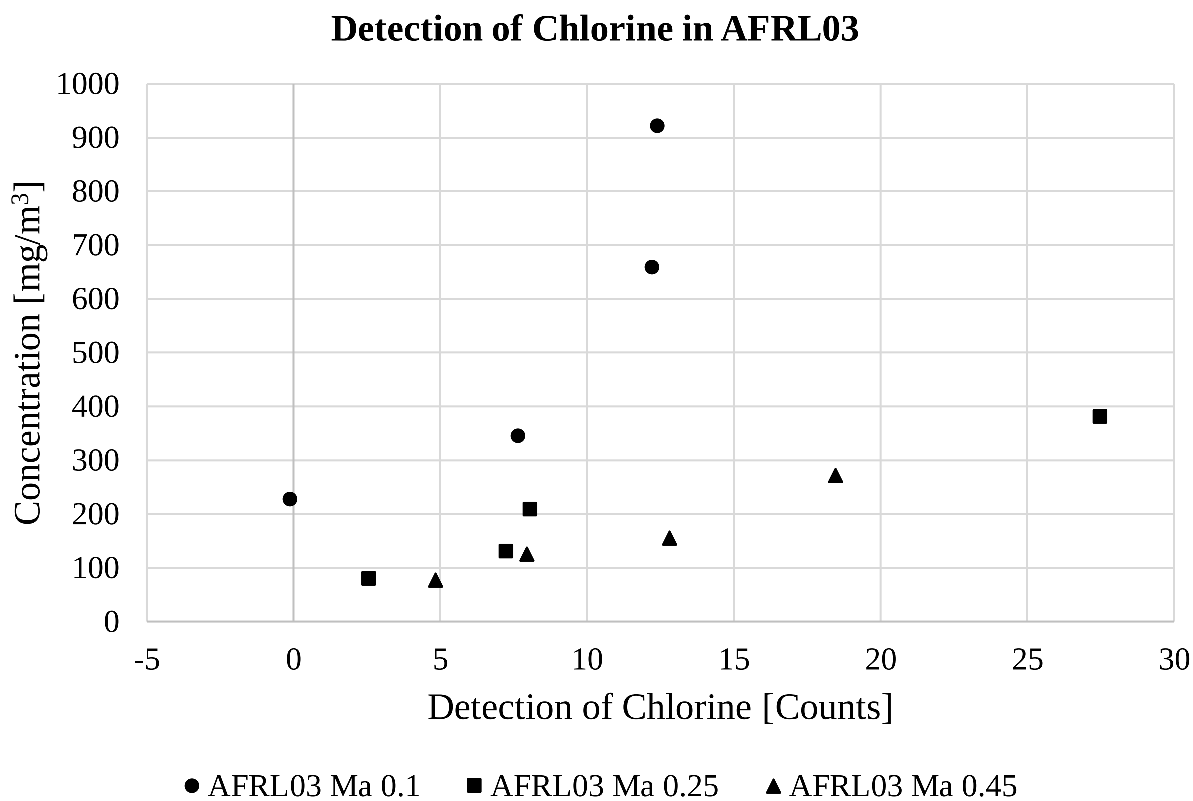

Figure A.5: XRF detection of Chlorine for AFRL03.

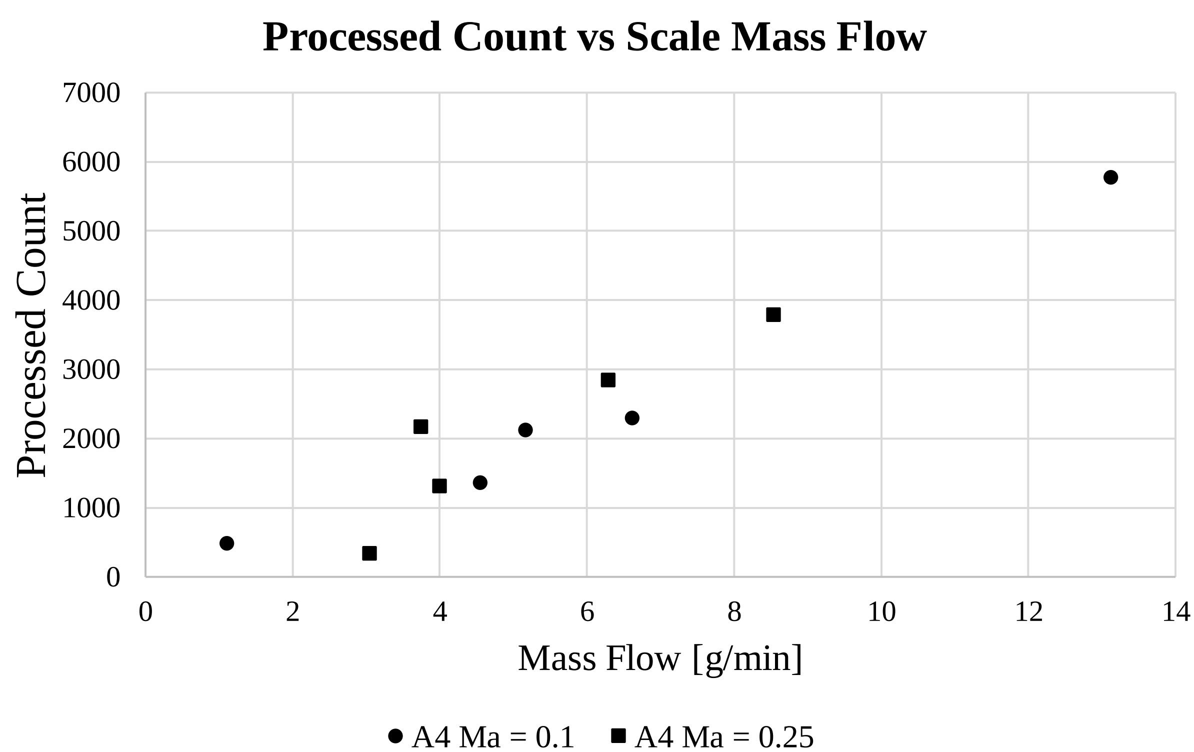

Figure A.6: OPS particle processed counts vs sand mass flow for ARD A4.

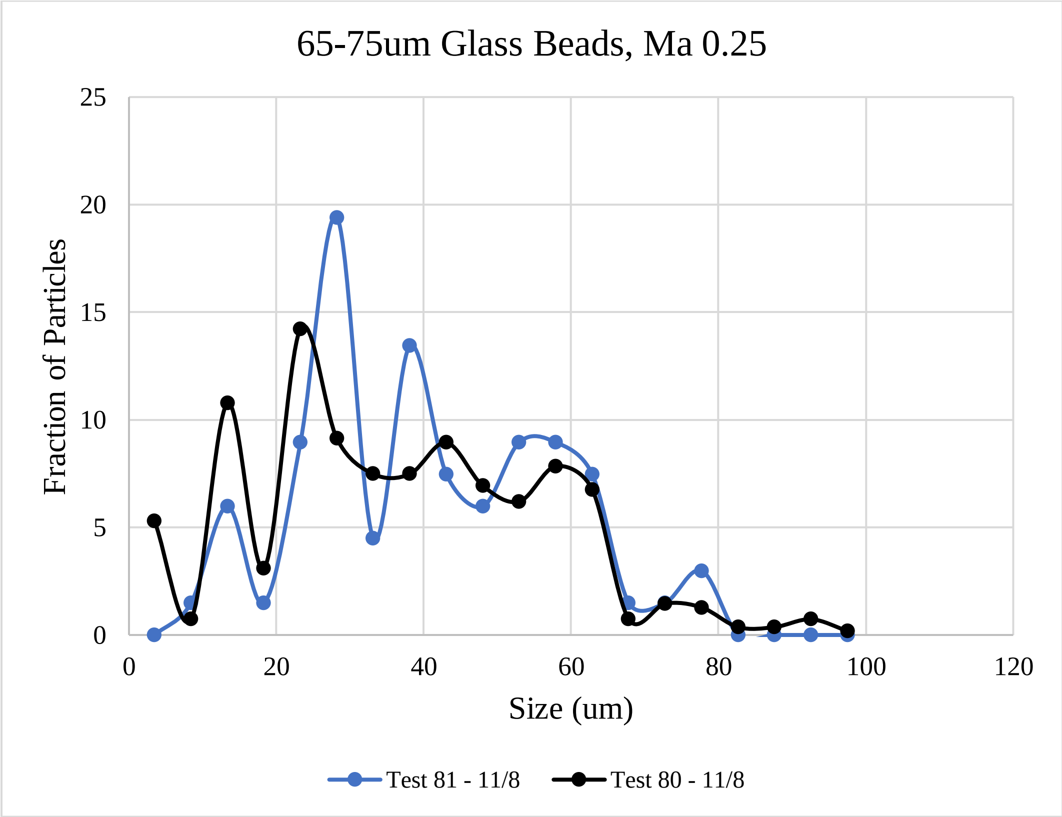

Figure A.7: OPS size distribution measurements for 65-75um glass microspheres.

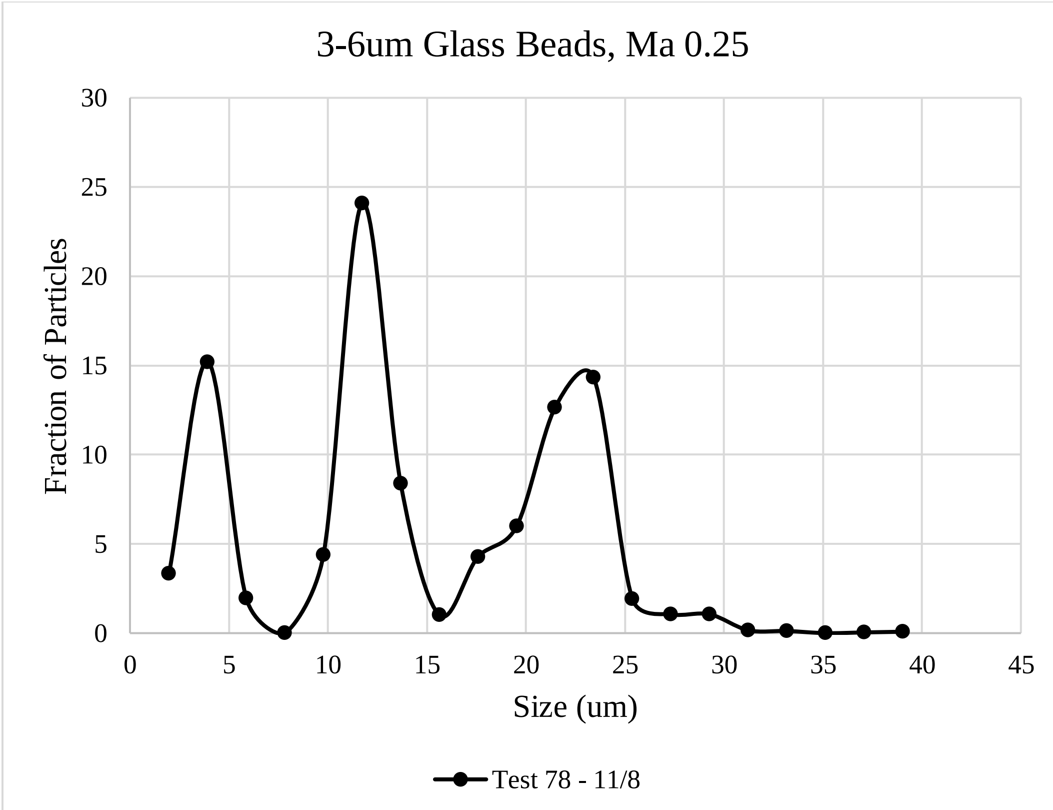

Figure A.8: OPS size distribution measurements for 3-6um glass microspheres.

Table A.1: Comparison of OPS and ParVis concentration variation to a regression line.

	Ma = 0.1		Ma = 0.25	
Parvis Cameras	*Single*	*Multi*	*Single*	*Multi*
RMS of ParVis Concentration Deviation to Trendline [mg m^{-3}]	72	39	255	52
RMS of OPS Concentration Deviation to ParVis Trendline [mg m^{-3}]	372	194	323	175

B Second Appendix

Figure B.1: HSWT rig including the sand feeder purge box.

Figure B.2: HSWT rig.

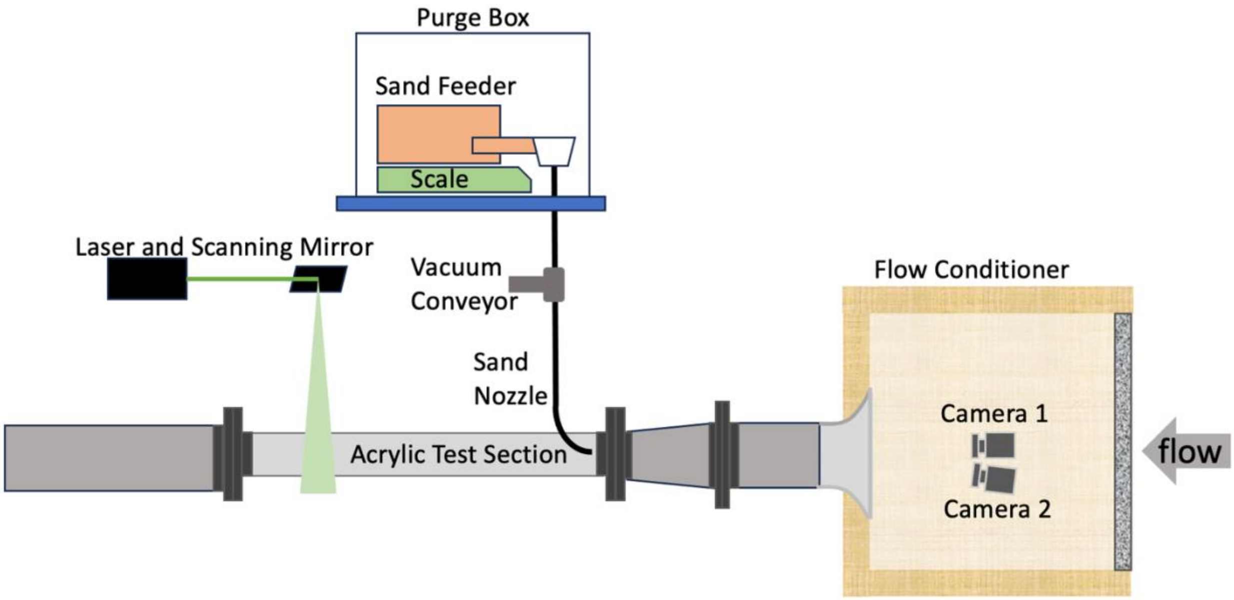

Figure B.3: HSWT diagram with camera locations.

Figure B.4: OPS and XRF probe mounted to the acrylic test section.


Figure B.5: OPS sensor mounted to the test section.

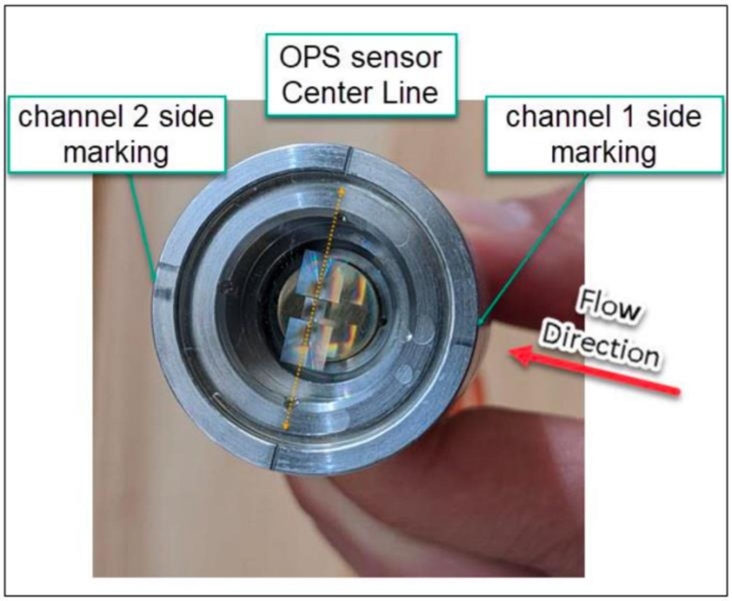

Figure B.6: OPS sensor diagram.

Figure B.7: Sand feeder on weight scale.

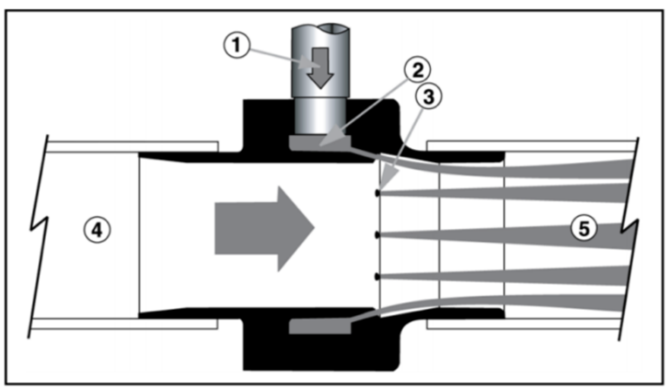

Figure B.8: Exair Corp. vacuum conveyor diagram.

Figure B.9: Sand feeder control box.

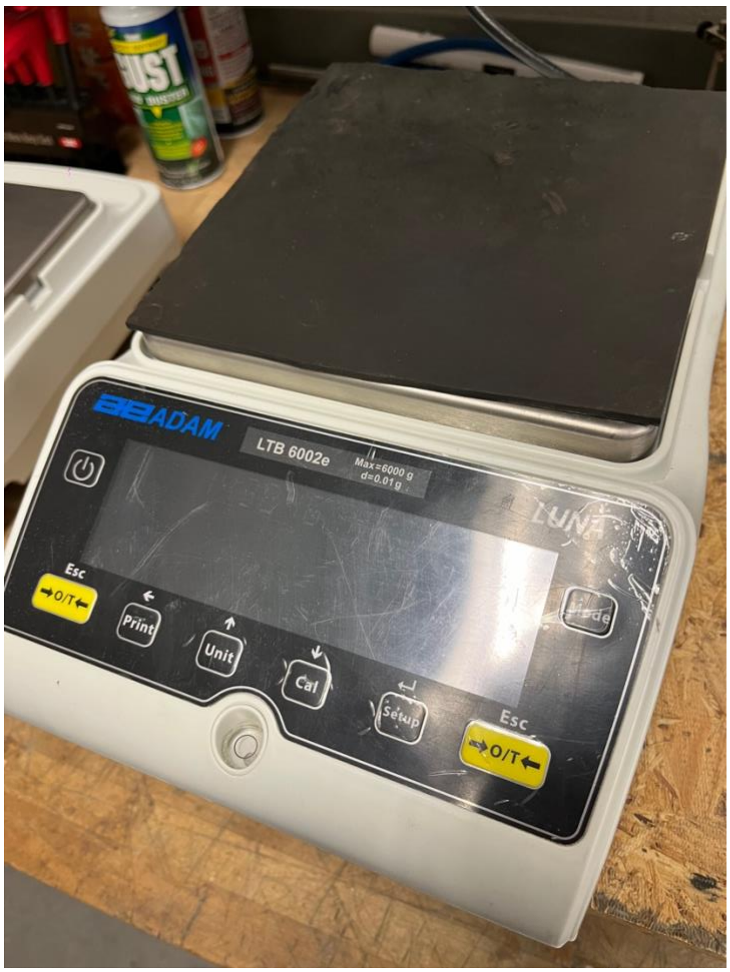

Figure B.10: Weight scale used for sand mass flow measurements.

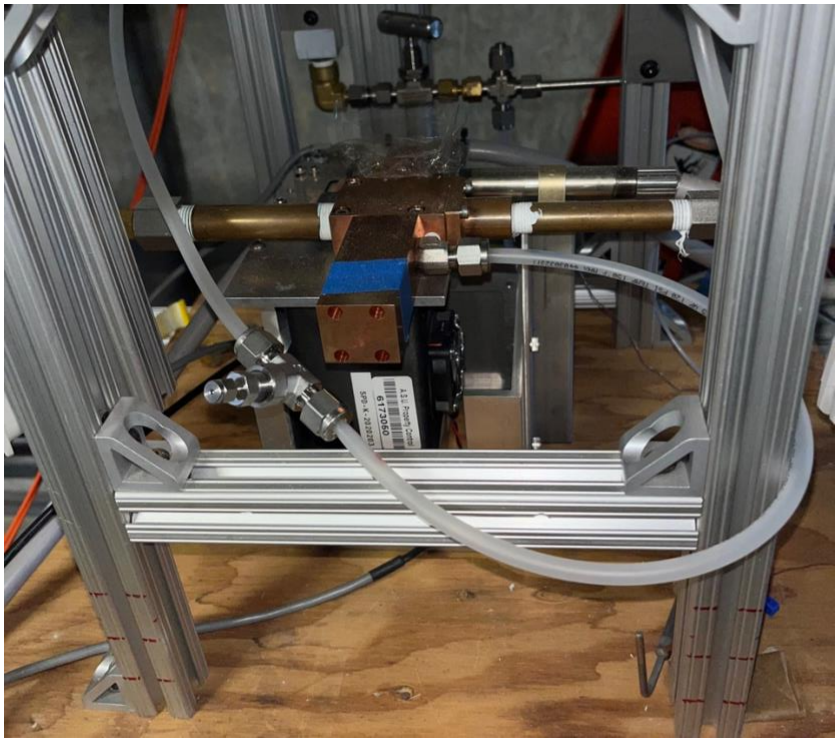

Figure B.11: XRF sensor.

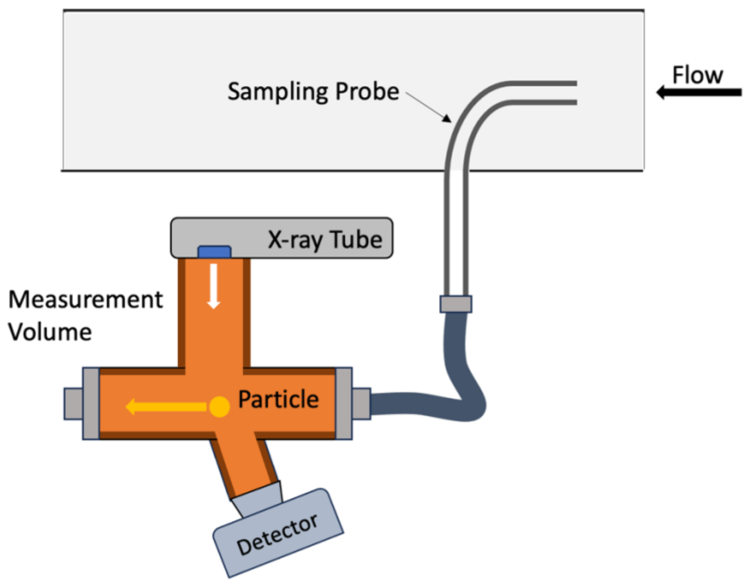

Figure B.12: XRF sensor diagram.

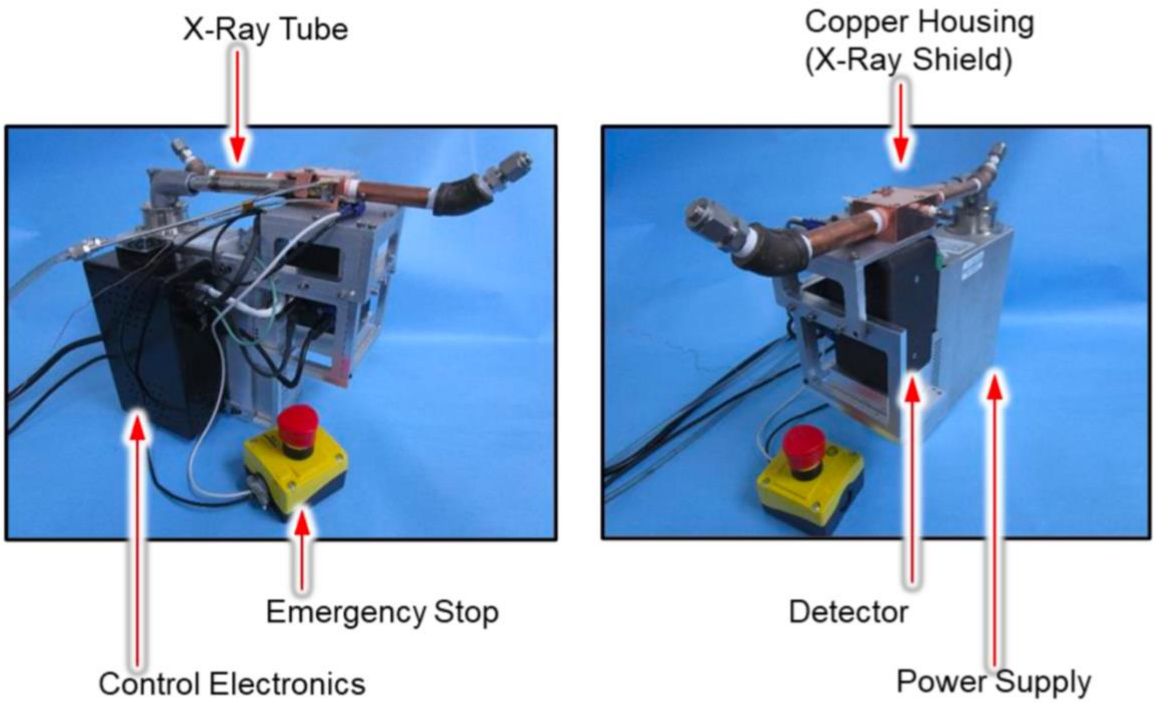

Figure B.13: XRF sensor diagram.